1. DISORDER-ENHANCED SUPERCONDUCTIVITY

M. Belogolovskii[1, 2, 3], A. Shapovalov[1], E. Zhitlukhina[2, 4], P. Seidel[3]

Abstract

Correlation between superconductivity and disorder remains an intriguing and challenging puzzle in condensed matter physics. According to the Bardeen–Cooper–Schrieffer (BCS) theory, the superconducting phenomenon emerges due to the binding of mobile electrons into Cooper pairs that forms a macroscopic quantum coherent state. For a weakly disordered system, the well-known Anderson theorem states that superconductivity is insensitive to disorder factors, such as elastic scattering centers, not affecting the time-reversal symmetry. Nevertheless, this statement is valid only for initially isotropic, homogeneous, and weak-coupling materials. It was shown that for a variety of non-uniform superconducting structures, the homogenization of the superconducting pair potential should result in the degradation of superconducting properties. Later, it was found that the naive expectations of unaffected or suppressed superconductivity in disordered materials, in general, are inappropriate. Due to these findings, nowadays attention is mainly focused on measuring and explaining *disorder-enhanced superconductivity.* This chapter updates the research status of such activities and presents some original results in this field obtained by the authors. The materials discussed below are classified according to their structural order. Two extreme cases are crystalline binary alloys with a periodic translation of a single unit cell (long-range order) and amorphous compounds with the appreciable degree of short-range or even medium-range order and the lack of inherent periodicity. Concerning solid-solution crystalline binary alloys, we focus on an enhancement of properties unexpected for a simple mixture of constituent elements. We argue that the amorphous structure made the requirement of substrate-film lattice matching, typical for crystalline layers, unnecessary thus providing good adhesion of amorphous films to different substrates. An intermediate case between the two extremes is high-entropy alloys, multi-component materials in which five or more elements randomly occupy a certain crystallographic site. Such highly atomic-disordered state produces many superior mechanical and / or thermal

characteristics (in particular, superconducting electrical properties), which are robust against atomic disorder or extremely high pressure. We are also discussing an effect of the structural disorder on the vibrational spectrum of superconducting materials and discuss possible explanation of disorder-enhanced superconducting properties in the framework of traditional phonon-mediated strong-coupling superconductivity.

✉ Mikhail Belogolovskii
belogolovskii@ukr.net

[1] Kyiv Academic University, Academician Vernadsky Blvd. 36, 03142 Kyiv, Ukraine

[2] Vasyl' Stus Donetsk National University, 600-richchia vul. 21, 21021 Vinnytsia, Ukraine

[3] Institut für Festkörperphysik, Friedrich-Schiller-Universität Jena, Helmholtzweg 3, 07743 Jena, Germany

[4] O. O. Galkin Donetsk Institute for Physics and Engineering, National Academy of Sciences of Ukraine, Nauki Ave. 46, 03028 Kyiv, Ukraine

1.1 Introduction

First study of the disorder effect on superconductivity was carried out in the 1930s by Shalnikov [1.1]. This activity was revived again in the late 1950s by Anderson [1.2] and Abrikosov and Gor'kov [1.3]. According to Anderson, dilute elastic scattering centers (impurities, dislocations, etc.), which could not affect the time-reversal symmetry, have no significant effect on thermodynamic properties and pair potential of three-dimensional *s*-wave BCS superconductor with a good crystalline structure (this statement is known in the literature as Anderson theorem). In contrast, as shown by Abrikosov and Gor'kov, magnetic impurities of arbitrary concentration may destroy superconductivity. However, when disorder reaches a critical level that can induce the localization of the electron wave function, a quantum phase transition, usually termed a superconductor-insulator transition, is emerging [1.4, 1.5]. Therefore, study of dirty superconductors gives a unique possibility to analyze competition between Cooper pairing of electrons and their Anderson localization arising due to intensive scattering processes from dopant centers.

How does superconductivity behave when the amount of disorder in the studied material is increasing? The answer to this question has been discussed in a number of reviews [1.6, 1.7, 1.8]. It was found that similar to many physical and chemical characteristics such as mechanical, electrical, magnetic, thermal, *etc.* superconducting properties reveal marked changes with disorder, as well. New aspects of this problem include, for example. quasi-1D systems which can exhibit long-range order at low temperature, but are heavily influenced by disorder [1.9, 1.10] and quasi-2D monolayers where the unusual enhancement of T_c was attributed to the multifractality of electron wavefunctions [1.11]. Some important conclusions can be drawn by analyzing experiments with strongly correlated superconductors, in particular, with high-T_c cuprates. A sharp increase in the critical temperature was found to be accompanied by the suppression of charge density waves, which indicates a strong competition between them and a still unknown mechanism of the high-temperature phenomenon [1.12]. On the other hand, the Van Hove scenario for HTSC [1.13, 1.14] was shown to be valid even for weak disorder [1.15].

As a result of joint efforts, our understanding of dirty superconductors has changed a lot over the past few decades. In particular, it became evident that

the Anderson theorem is applied only to initially isotropic, homogeneous, and weak-coupling materials. A specific case of a system without translational symmetry where the Anderson theorem is not satisfied is a normal-metal (N) film proximitized to a superconductor [1.16]. Its inapplicability shows up, first, in the homogenization of pair potentials over the N and S layers that becomes evidently lower than that in a pure S material. This conclusion, in fact, is valid not only for N/S bilayers but also for a variety of inhomogeneous weakly disordered superconducting structures. It is remarkable that the results by Arnold [1.16] for very thin N and S layers bear a striking resemblance to the McMillan tunneling model [1.17] of the proximity effect for two N and S layers separated by a tunnel barrier. The correspondence arises from a similar treatment of lifetime effects. It is also not surprising that analogous expressions are appropriate for multiband superconductors with nonmagnetic impurity scattering treated within the Born approximation [1.18, 1.19]. As in the common case of an anisotropic superconductor [1.20], interband scattering reduces the critical temperature T_c and finally leads to a *single* order parameter, in overall agreement with previous studies [1.21].

In general, the effect of impurities and / or defects on the properties of a primary superconductor is strongly material-dependent, compare the data for ferro-pnictides [1.22], amorphous molybdenum silicon these films [1.23], niobium titanium nitride films [1.24], oxide interfaces [1.25], or nanostructured Sn samples [1.26]. In most cases, the traditional design of novel superconductors started from a primary or host substance, to which a new component or components were added for improving the material performance. The above naive expectations that in this case T_c should remain unaffected or can only decrease, was found inappropriate, and nowadays a lot of attention is focused just on measuring and explaining ***disorder-enhanced superconductivity*.** For example, many of actual transition-metal alloys with attractive superconducting properties have been found to be located in the centers of the phase diagrams rather than close to its corners. The second subsection of the overview illustrates this observation with an example of binary Mo-based alloys. Another case of extreme disorder is an amorphous (structurally disordered, i. e., disordered in the spatial arrangement of atoms) superconducting phase stabilized in the form of thin films by some metals and metallic alloys.

The discovery of superconductivity in the amorphous phase dates back to early 1950's when quench condensed films of amorphous Bi were reported to be superconducting with T_c = 6.1 K [1.27] in contrast to crystalline Bi that is a superconductor with the critical temperature of 0.53 mK [1.28]. It was claimed that the superconductivity in amorphous Bi results from its higher packing density than crystalline Bi [1.29] but convincing experimental evidence was absent. Later it was found that some elements which are non-superconducting at all, such as Be [1.30], become superconducting in the amorphous state [1.29, 1.31]. At the same time, other elements like Pb are good superconductors in the crystalline phase while disorder lowers T_c. We present some results for amorphous superconducting compounds including original ones and discuss them in the third subsection of the chapter.

From the fundamental point of view, the most important task in the study of disorder-enhanced superconductivity remains to answer the question – why T_c's of highly disordered superconductors quite often exceed those of the crystalline counterparts. In the paper [1.32], the authors proposed two possible mechanisms for increasing the superconducting transition temperature T_c by nonmagnetic disordering factors in both conventional and unconventional (sign-changing gaps) superconductors. In the first scenario, relevant to multi-band systems, the origin of the T_c growth is the density-of-states enhancement driven by resonant states in near-Fermi-level bands while the second one applicable to systems close to localization it is related to random disorder-generated local density-of-states modulations. In the third subsection of the overview, we argue that superconductivity in such materials is usually strongly (or at least moderately) coupled, with the electron-phonon coupling parameter $\lambda \geq 1$ and the superconducting gap Δ much larger than its value predicted by the BCS theory: $\Delta = 1.76 k_B T_c$. It means that we should look for the fundamental explanation of these findings within the framework of the Eliashberg theory of strong-coupling phonon-mediated superconductivity [1.31], using details depending on the nature of the disorder and superconductor pairing symmetry. This issue is discussed at the end of the third subsection.

The novel tendency in studying disorder-enhanced properties is concentrated not on the materials formed by a single host and an additional component as those discussed in the second subsection but rather on compounds with

multiple elements which crystallize as solid solutions. In such systems known as high-entropy alloys (HEA), the structural order / disorder can be characterized through the entropy, a measure of the randomness. Such alloys composed typically of four or more components are usualy characterized by simple structures with extremely high chemical disorder and high entropy of mixing stabilizing the crystal structure and resulting in highly tunable properties [1.33–1.36]. The highly atomic-disordered HEA state produces many superior mechanical and / or thermal characteristics. Superconductivity has become one of the most important topics in this field since the discovery of a bcc HEA superconductor in 2014 [1.37]. Our fourth subsection is dealing with superconducting high-entropy alloys, which are expected to be useful for realizing the relationship between crystalline and amorphous superconductors.

1.2 Solid-solution crystalline binary alloys: is the rigid band approximation adequate?

A binary superconducting alloy is a mixture of two chemical elements of which at least one is a metal element forming a substance with conducting characteristics. The most common and oldest alloying process is performed by heating the base metal beyond its melting point and then dissolving the solutes into the molten liquid even if the melting point of the solute is far greater than that of the base. By adding another element to a metal, differences in the size of the atoms create internal stresses in the lattice of the metallic crystals, which sometimes enhance its properties.

Understanding electronic characteristics of binary random alloys has become a topic of considerable interest in solid-state physics. The first two approximations used in the study of these compounds were rigid band and virtual crystal approximations, which are valid for the case when a periodic crystal structure of the materials discussed is well defined. Even oversimplified, they can nevertheless suggest a way allowing the development of alloys with properties tuned for specific applications, in particular, when they depend on variations in Fermi surface topology induced just by alloying. The rigid band model, in which the band structure and density of states of the solvent metal remain unchanged upon alloying with a solute allows predict these

variations [1.38]. Although the rigid band behavior has been confirmed for many nearly free electrons and some systems with transition metals [1.39–1.41], its applicability remains questionable, especially when the solute strongly perturbs the local electronic structure of the solvent [1.42]. From this viewpoint, understanding the physical properties of simple binary random alloys is very useful for facilitating a detailed picture of the development of conduction states in complex alloys containing transition metals. As an example, we will discuss below the evolution of a band structure and the Fermi surface of $Mo_{1-x}Re_x$ alloy in normal and superconducting states as functions of its composition.

As for the normal state, we refer to the work [1.43] where the authors presented detailed experimental and theoretical study of the electronic structure of $Mo_{1-x}Re_x$ random alloys. They measured electronic band dispersions for clean and hydrogen-covered $Mo_{1-x}Re_x$ alloys with $x = 0 - 0.25$ using angle-resolved photoemission spectroscopy and performed numerical calculations by the Korringa–Kohn–Rostoker coherent-potential-approximation method, a simplest self-consistent approximation. In the latter approach, one regards the total scattered wave as composed of contributions from each atom while the effective wave incident on a given atom excludes its own effect. The result is a product of the atomic *t*-matrix and the effective wave [1.43]. As for the superconducting state, its analysis is based on our previous publications [1.44–1.45].

Re ($5d^5 6s^2$) has one more electron per atom than Mo ($4d^5 5s^1$), which in the rigid band approximation would be shared with the molybdenum host. The authors [1.43] found that with increasing Re concentration, bulk and surface electronic bands are shifting away from the Fermi energy E_F due to two factors: (i) the aforementioned charge donation and (ii) increase in the occupied bandwidth, most notably for bands more than 2 eV below E_F, see Fig. 1.1. However, this effect is not uniform, with larger shifts observed at higher binding energy. Two other deviations from rigid band behavior were as follows: (i) a surface-localized state shifted in a notably non-rigid way and (ii) spin-orbit interaction impact increased with growing rhenium concentration, again leading to non-rigid modifications of some bands.

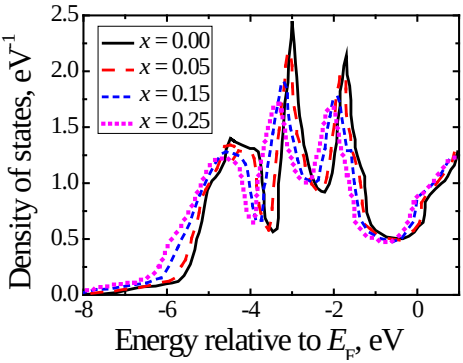

Fig. 1.1 – Configurationally averaged density of electronic states of $Mo_{1-x}Re_x$ random alloys (x = 0.00, 0.05, 0.15, and 0.25) calculated using the Korringa–Kohn–Rostoker coherent-potential-approximation method. Adapted from Fig. 1 in Ref. [1.43]

The authors [1.43] also revealed an electronic topological transition which may impact many physical properties of alloys. It occurs when the Fermi surface changes its topology as E_F is moving through a van Hove singularity in the density of states $N(E_F)$. This idea is traced back to the work by Ilya Lifshitz who related a change in the topology of the Fermi surface $E(\mathbf{p}) = E_F$ of a pure metal subjected to elastic strains to anomalies in thermodynamic quantities of metals [1.46−1.48]. The effect is arising due to the continuous variation of some parameter (*e. g.*, pressure or impurity concentration), due to which the difference $z = E_F - E_c$ between the Fermi energy E_F and the critical energy E_c, at which the topology of the constant energy surface is changing, passes through zero continuously. This leads to the modification in the Fermi-surface connectivity, for example, an appearance of a new cavity or the rupture of a connecting neck with varying external parameter. At the temperature T = 0 K, the grand thermodynamic potential Ω acquires an irregular correction $\delta\Omega = -\alpha|z|^{5/2}$ and that is why this effect was also called the phase transition of the 2.5-order [1.47], referring in this case to the Ehrenfest terminology. At $k_BT \ll E_F$, related anomalies manifest themselves not only in thermodynamic characteristics of metals, but also in superconducting parameter-versus-z dependencies, as was evidenced by Brandt *et al.* in the paper [1.49] just by analyzing pressure induced changes in the properties of superconducting Tl–Hg alloys.

In fact, topology and alloying are often closely intertwined in condensed matter physics. In both cases, one seeks to characterize not the details of a

particular band structure or disorder configuration, but the basic physics of the phenomenon. Returning to the $Mo_{1-x}Re_x$ alloys, we are referring to detailed first-principles calculations of their bulk electronic structure by Skorodumova *et al.* [1.41] who predicted two Lifshitz topological transitions at 2 % and 6 % Re concentrations occurring near the middle of the N–H line in the bulk Brillouin zone. Comparison of Fermi surfaces for pure Mo and $Mo_{0.75}Re_{0.25}$ in Ref. [1.43] confirmed it by revealing the van Hove singularity at 5 % rhenium concentration, i. e., very close to the theoretical predictions [1.41]. Recent results of resonant photoemission spectroscopy experiments [1.50] proved the existence of two electronic topological transitions at critical Re concentrations of $x_{c1} = 0.05$ and $x_{c2} = 0.11$.

It is known that the addition of rhenium to molybdenum improve the ductility of the material. The stress required to produce a fixed amount of strain higher than 3 % is minimal around $x = 0.07$ [1.51]. Smith et al. [1.52] found phonon softening along the N–H direction of the Brillouin zone when Mo-Re alloys undergo the Lifshitz transition and it is just the location of a Fermi surface pocket that appears when more than 5 at. % of rhenium is added to molybdenum [1.43]. Electronic states of the small group of carriers are localized due to the random potential introduced in the system when the composition is changed [1.53]. This effect is expected to be very small and its detection should require extremely sensitive techniques. Nevertheless, Ignat'eva [1.53] revealed large oscillations in the pressure dependence of T_c and in temperature derivatives of the normal-state thermoelectric power and resistivity. She argued that the localization of electrons filling the new states arising due to the topological changes of the Fermi surface causes the observed oscillations in related characteristics. The localized states against a background continuum give rise to Fano resonance in photoemission spectroscopy measurements detected in the $Mo_{1-x}Re_x$ system for $x > x_{c1} = 0.05$ [1.50]. This observation was interpreted as the result of the electron-like states localization in the newly appeared Fermi pocket. Next, let us discuss how the changes in the topology influence superconducting properties of the Mo-Re alloys and why it may considerably enhance the transition temperature to the superconducting state.

From the superconductivity viewpoint, it is important that the proximity of the Fermi surface to van Hove singularities drastically enhances interaction effects and can lead to the emergence of a flat band, where all the states have

the same energy. Since the flat band has a huge density of electronic states, this may considerably increase the transition temperature T_c. Notice that in ordinary superconductors, the singular density of electronic states emerging at the transition point generates non-analytical behavior of superconducting parameters as a function of the external factor modifying the shape of the Fermi surface [1.47]. In the paper [1.54], the authors presented a detailed study of temperature and magnetic field dependences of the magnetization M and heat capacity C in $Mo_{1-x}Re_x$ alloys with x = 0.25 and 0.4, *i. e.*, above two topological transitions in the Fermi surface. Notice that the $Mo_{0.6}Re_{0.4}$ alloy was identified as a strong coupling superconductor with the ratio of an energy gap $\Delta_0 = \Delta(T = 0)$ to the critical temperature $2\Delta_0/k_BT_c = 5.0$, that is well above the value of 3.52 predicted by the BCS theory of a weakly coupled superconductor (Fig. 1.2). The normalized values $\Delta C_S/\gamma T_c$ of the heat capacity ΔC_S jump at T_c (γT is an electronic contribution to the normal-state heat capacity) are about 1.7 and 2.0 for the $Mo_{0.75}Re_{0.25}$ and $Mo_{0.60}Re_{0.40}$ samples studied in the work [1.54], respectively. These values are also substantially higher than the BCS value of 1.43 pointing out again that superconductivity in the binary random $Mo_{1-x}Re_x$ alloys with $x > x_{c2}$ is at least nontrivial as it follows from the electron-phonon coupling constant-vs-Re concentration dependence, see Fig. 1.2.

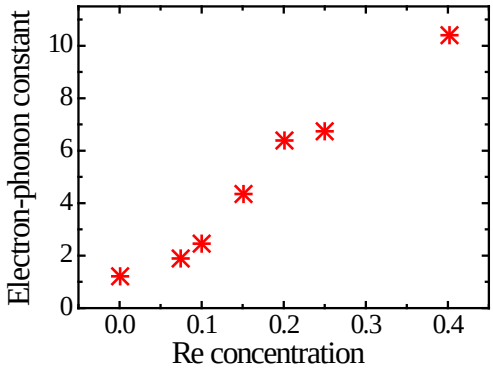

Fig. 1.2 – Variation of the electron-phonon coupling constant λ as a function of Re concentration x in $Mo_{1-x}Re_x$ alloys. Adapted from Fig. 5 in Ref. [1.55]

Fig. 1.1 demonstrates the fundamental possibility of using the rigid band model for a qualitative description of changes in the electronic structure of random binary alloys with increasing the solute concentration, while Fig. 1.2

shows a strong enhancement of the electron-phonon interaction coupling for large Re concentration. The question arising is if it is possible to predict minor details in the electronic structure, such as relatively small changes in the Fermi surface topology. For example, do predicted two Lifshitz topological transitions at small Re concentration [1.41] really exist? As was explained above, the opening of a new cavity in the Fermi surface can lead to the appearance of an additional energy gap in the spectrum of single-particle excitations of a superconductor studied. Can we detect it?

Unfortunately, the identification of a second gap can be extremely problematic. Fig. 1.3 exhibits the temperature dependence of the ratio $\Delta C_S/\gamma T_c$ for two Mo-Re compounds studied in Ref. [1.54]. Dotted lines in Figs. 1.3a and 1.3b represent $C_S(T)$ behavior in the superconducting state with a single isotropic superconducting gap $\Delta_0/k_B = 19.0 \pm 0.5$ K for the $Mo_{0.75}Re_{0.25}$ alloy and $\Delta_0/k_B = 26.5 \pm 0.6$ K for the $Mo_{0.60}Re_{0.40}$ alloy.

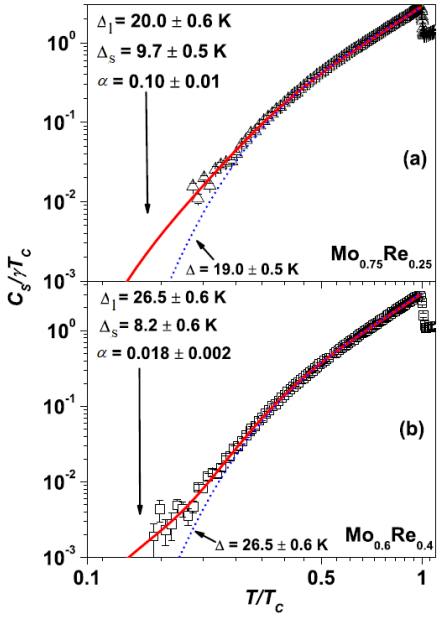

Fig. 1.3 – Temperature dependences of the electronic heat capacity in the superconducting state plotted as a function of the ratio T/Tc for Mo0.75Re0.25 (a) and Mo0.60Re0.40 (b) samples. The lines are fits to the experimental data (open symbols) within single-gap (dotted lines) and two-gap (solid lines) theoretical approaches. Adapted from Fig. 7 in Ref. [1.54]

We can see that experimental values of $C_S(T)/\gamma T_c$ at low temperatures are systematically higher than calculated ones. Realizing this, the authors of Ref. [1.54] tried to fit the experimental data using an equation for a two-band superconductor

$$\frac{C_S(T)}{\gamma T_c} = \alpha \frac{C_{Ss}(T)}{\gamma_s T_c} + (1-\alpha)\frac{C_{Sl}(T)}{\gamma_l T_c} \tag{1.1}$$

with $C_{Ss}(T)$ and $C_{Sl}(T)$, contributions to heat capacity from a small Δ_s and a large Δ_l superconducting gaps, $\alpha = \gamma_s/(\gamma_s+\gamma_l)$ defines the fraction of the small gap, $\gamma_{s,l}$ are related normal-state coefficients. They found that the resulting lines are perfectly consistent with the measured $C_S(T)$ data, see solid lines in Fig. 1.3 where the values of Δ_s, Δ_l, and α are specified. Notice that a clear deviation from the single-gap behavior was observed already in an earlier study of the temperature dependence of electronic heat capacity in $Mo_{0.60}Re_{0.40}$ alloy [1.56] but was ignored. Now it is evident that the discrepancy between theory and experiment can be removed by taking into account the presence of *two superconducting gaps*.

Magnetization-vs-external magnetic field measurements at various temperatures made it possible to estimate the upper critical field $H_{c2}(T)$ dependencies as the field in the isothermal *M-H* curves at which the irreversible (giving rise to a hysteresis loop) magnetization *M* reduces to zero. It was found that the temperature impact on H_{c2} estimated using the Werthamer–Helfand–Hohenberg model matches with the experimental curves only at temperatures close to T_c. The lower critical field H_{c1}, below which a type-II superconductor is in the Meissner state, was found analyzing *dM*(*H*)*/dH* dependencies. For a superconductor in the local limit with $\xi(0) << \lambda$, $\xi(0)$ and λ are coherence length and London penetration depth, the normalized superfluid density $\rho_S(T)$ reads as [1.54]

$$\rho_S(T) = \frac{\lambda^2(0)}{\lambda^2(T)} = \frac{H_{c1}(T)}{H_{c1}(0)}. \tag{1.2}$$

For a single gap superconductor, $\rho_S(T)$ is given by [1.57]

$$\rho_S(T) = 1 + 2\int_0^\infty N_S(\varepsilon,T)(df(\varepsilon,T)/d\varepsilon)d\varepsilon \tag{1.3}$$

with the Fermi-Dirac distribution function $f(\varepsilon)$ and the normalized density of single-particle states in a superconductor [1.58]

$$N_S(\varepsilon,T) = \mathrm{Re}\left(\varepsilon / \sqrt{\varepsilon^2 - \Delta(T)^2}\right), \qquad (1.4)$$

$\varepsilon = E - E_F$. Dotted lines in Figs. 1.4a and 1.4b show the temperature dependence of normalized superfluid density calculated using Eq. (1.3) for an isotropic single-gap superconductor with $\Delta_0/k_B = 15.5 \pm 0.5$ K for the $Mo_{0.75}Re_{0.25}$ alloy and $\Delta_0/k_B = 20.5 \pm 0.4$ K for the $Mo_{0.60}Re_{0.40}$ alloy. Similar to Fig. 1.3, the estimated theoretical curve matches well with the experimental data at high temperatures while a marked deviation observed at low temperatures indicates possibility of the two-gap superconductivity. Acting like above for the heat capacity exhibiting an anomalous feature in its temperature dependence, see Eq. (1.1), the authors [1.54] got an excellent agreement between the measured and calculated curves with the parameters Δ_s, Δ_l, and α indicated in Fig. 1.4. These values noticeably differ from those in Fig. 1.3. Possibly, this is caused by the fact that the superfluid density estimated from H_{c1} is a local property whereas heat capacity is a bulk (that is, averaged) characteristic [1.54].

Nevertheless, the above arguments supporting a two-band / two-gap scenario in superconducting random Mo-Re alloys (Figs 1.3 and 1.4) can only hint at the presence of two superconducting order parameters while it would be desirable to get the related information from the experiments that could provide direct evidence of the two gaps presence without additional calculations. Let us emphasize, that tunneling and point-contact spectroscopies schematically shown in Fig. 1.5 are exactly such techniques allowing one to interpret the measured differential conductance characteristics qualitatively without resorting to complicated model concepts [1.58]. As well known, related spectroscopic setups usually consist of two metallic electrodes (at least, one of them is in the superconducting state) divided by resistive nanometer-scale region. Its task is to take over the entire voltage drop V applied to the setup creating thus a difference $\Delta\mu = \mu_L - \mu_R$ in chemical potentials of the left (L) and right (R) electrodes. Modifying the drop V value, we are changing the difference $\Delta\mu = eV$ and thereby are able to probe unoccupied and occupied states in the excitation spectra of the conducting electrodes.

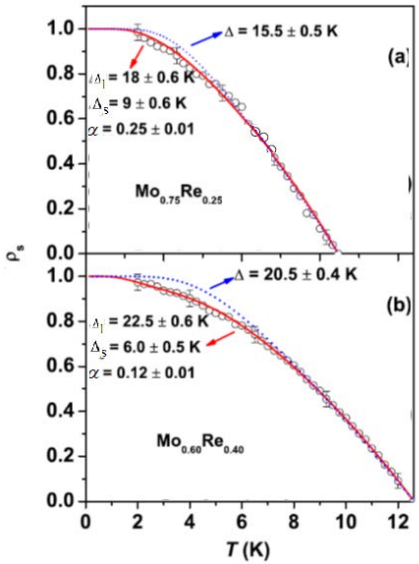

Fig. 1.4 – Temperature dependences of the superfluid density of states plotted as a temperature function for Mo0.75Re0.25 (a) and Mo0.60Re0.40 (b) samples. The lines are fits to the experimental data (open symbols) within single-gap (dotted lines) and two-gap (solid lines) theoretical approaches. Adapted from Fig. 6 in Ref. [1.54]

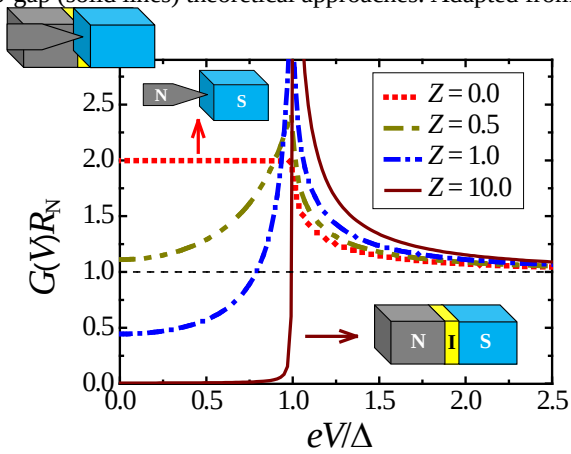

Fig. 1.5 – Simulated differential conductance–versus–voltage curves for zero-temperature coherent quantum transport across a one-dimensional normal metal-barrier-superconductor trilayer with various barrier transparences. Their shapes are controlled by the parameter Z. Two extreme limits, corresponding to a point contact (Z = 0) and a tunnel junction (Z >> 1), are illustrated schematically

Applying this idea, two extreme junction-spectroscopy techniques (tunneling and point-contact) differ only in the ways of creating the interlayer between two metals often called a weak link. A simplest, from the realization viewpoint, version of the high-resistive interlayer is a narrow constriction between two wide electrically conducting regions, whose width is comparable to the electronic wavelength λ_F, see the inset in Fig. 1.5. The conductance G of such device known as a quantum point contact can be as small as $G_0 = 2e^2/h \approx$ 77.5 μS, the universal conductance quantum [1.59]. This relation is valid for truly atomic dimensions when two bulk metals, reservoirs of electrons in local equilibrium, are connected by a quasi-one-dimensional single-atom constriction [1.60]. The G value grows with increasing the width w of the electron waveguide through which a small integer number of transverse modes $N \approx 2w/\lambda_F$ can propagate at the Fermi level E_F.

Tunneling spectroscopy that played a central role in the experimental verification of the microscopic theory of superconductivity in traditional superconductors represents an opposite case of the interface transparency. Conventional tunnel junction shown schematically as an inset in Fig. 1.5 is planar with a several nm-thick oxide interlayer, an area prohibited by classical mechanics for electrons at the Fermi level of electrodes and for this reason often named a barrier. Hence, the difference between two main techniques is to a great extent quantitative, namely, transition probabilities for charges to be transferred between junction electrodes in a certain quantum channel is near unity for the point-contact spectroscopy while it is much less than unity in the tunneling approach [1.61].

The most popular model to calculate the differential conductivity $G(V) = \mathrm{d}I(V)/\mathrm{d}V$ (the derivative of the current I across the contact with respect to the voltage V applied to it) of the normal metal-barrier-superconductor contact with a barrier of arbitrary transparency is that proposed by Blonder, Tinkham, and Klapwijk (BTK) [1.61]. The model assumes ballistic and one-dimensional character of the charge transport through the contact of N and S metals with a nanometer-thin scattering potential localized at the N-S interface. Its effect is usually considered by introducing a potential barrier with a thickness d_B and the decay length l_B inside it. For a strong inequality $d_B << l_B$, transmission t and reflection r amplitudes read $t = i/(i - Z)$ and $r = Z/(i - Z)$, where i is the imaginary unit, see the details in the papers [1.62, 1.63].

Ultimately, the parameter Z determines the probability of electron transmission through the barrier $D = 1/(1+Z^2)$ in the normal state as well as its probability to be reflected back $R = 1 - D = Z^2/(1+Z^2)$. The way of further calculations aimed to find the ratio of differential conductance in superconducting $G_S(V)$ and normal G_N states is described in detail in the work [1.63]. Possible effect of inelastic-scattering processes in the superconductor is taken into account by introducing a constant imaginary part in the electronic energy $E \rightarrow E + i\Gamma$, where Γ is known as the Dynes parameter [1.64]. As a result, we have three adjustable parameters for a single-band superconductor, the energy gap Δ, the interface scattering efficiency Z, and the Dynes parameter Γ. In the case of a two-band superconductor, this number increases to seven: Δ_l, Δ_s, Z_l, Z_s, Γ_l, Γ_s and, finally, the weighting factor $w_l < 1$ ($w_s = 1 - w_l$), which specifies the relative contribution of the two bands to the measured curve $G(V) = w_l G_l(V) + w_s G_s(V)$ [1.64].

In point contacts, the channels with the highest transmission probability determine the current along the device and, as a result, the scattering strength Z is nearly zero. In this case, for an electron (hole) incident on the interface from the N side at energies less than the superconductor energy gap Δ, the ballistic throughput across an N/c/S point contact (c is the constriction) is dominated by a quantum process called Andreev reflection. Its details are as follows. Electron (hole), arriving from the N side, forms a Cooper pair in the S electrode reflecting back a hole (electron) from the electron band with opposite spin and group velocity to the incident electron (hole) but with almost equal momentum. It is clear that this effect causes an enhancement of the conductance below the superconducting energy gap Δ, and the ratio of below-gap and above-gap conductance values equals 2 for an ideal point contact with a conventional superconductor (Fig. 1.5).

With increasing Z, the shape of the differential conductance $G(V)$ for an N/I/S trilayer transforms from a flat section at $|V| < \Delta/e$ to peaks at $|V| = \Delta/e$. From Fig. 1.5 illustrating these changes at very low temperatures, it is clear that the Andreev-reflection mechanism, that defines the shape of the conductance spectrum for a point contact with $Z \approx 0$, as well as the tunneling transport allow us to interpret measured $G(V)$ curves and to reveal qualitatively the energy gap value without involving complex model concepts.

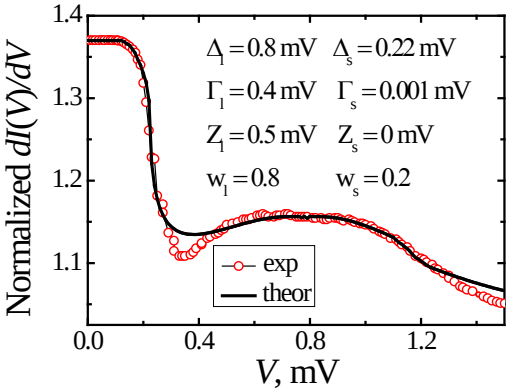

Fig. 1.6 – Normalized differential conductance–versus–voltage curve measured for a representative point-contact sample formed by a silver tip and a random Mo0.52Re0.48 alloy film (dots) compared with a fitting curve (solid line). The two energy gaps differ markedly: Δs = 0.22 meV and Δl = 0.8 meV, the contribution of the band with a larger gap Δl is dominant, the measurement temperature was 4.2 K

We have performed two different kinds of the junction-spectroscopy experiments using Mo-Re based tunneling trilayers [1.44] and point-contacts [1.45]. In the latter case, the N electrode was made of silver, its point contacts with the studied Mo-Re alloy were created both on film and bulk samples. Thin alloy layers with an approximately equal concentration of components, thicknesses ranging from 90 to 150 nm, and critical temperatures about 9 K were obtained by magnetron sputtering of a $Mo_{0.52}Re_{0.48}$ target. Structure and phase composition of the films were controlled by electron microscopy and electron diffraction, as well as by X-ray diffraction. The concentration of alloy components in the films determined using X-ray photoelectron spectroscopy with an accuracy of 5–6 at. % well corresponded to the target composition. Grain size spread was tiny. This uniformity revealed itself in high films resistance to structural transformations and stable electrophysical properties during thermal cycling. The measured differential conductance spectra $dI(V)/dV$ of contacts based on Mo-Re alloys with approximately equal component contents demonstrated the presence of two energy gaps, larger Δ_l and smaller Δ_s ones. Typical $G(V)$ curve shown in Fig. 1.6 represents a sum of two similar characteristics of N/S contacts with an almost ideal interface. The fitted parameters are indicated in Fig. 1.6. Notice that due to the

small area of contacts, we got an information only from individual micro-sized crystallites with different crystallographic directions, while, say, measurements of the electronic heat capacity for a molybdenum-rhenium alloy [1.54] provide characteristics averaged over all directions. Local changes in superconducting properties in the near-surface region may be a source of the differences between surface-sensitive techniques and those dealing with the bulk.

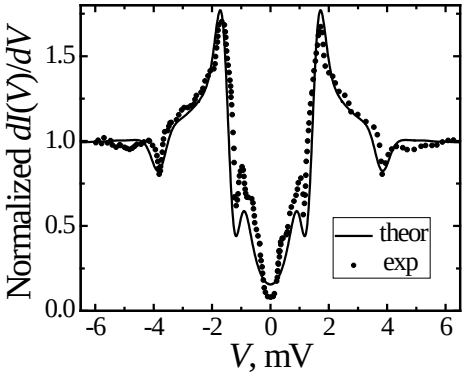

Fig. 1.7 – Normalized differential conductance–versus–voltage curve measured for a representative Pb/Al oxide/Al/Mo0.60Re0.40 tunnel junction (dotted curve) compared with a fitting curve (solid line). The energy gaps $\Delta s = 0.5$ meV and $\Delta l = 2.5$ meV reasonably agree with the values extracted from point-contact experiments, see Fig. 1.6, the contribution of the smaller-gap band was dominant, the measurement temperature was 4.2 K. Adapted from Fig. 2 in Ref. [1.44]

In Ref. [1.44], we presented our results for tunneling junctions based on $Mo_{0.60}Re_{0.40}$ polycrystalline films. The authors of Ref. [1.65] found that the native oxide of the Mo-Re alloy is grown up to thicknesses not more than 0.5 nm and are thinner that the oxides on Mo and Re surfaces. Therefore, in order to form a low-leakage tunnel junction on the Mo-Re film, they had to cover it with an Al overlayer, oxidized after that. Following the work [1.65], we have used artificial Al-oxide tunnel barriers and a 100 nm-thick lead counter-electrode to form low-leakage tunnel junctions for measurements in the gap region not carefully analyzed in the previous tunneling experiments [1.65]. If we are dealing with a two-gap superconducting electrode, $G(V)$ dependence for a tunnel junction should exhibit a two-peak structure. Fig. 1.7 demonstrates representative conductance spectrum of the Pb/Al oxide/Al/$Mo_{0.60}Re_{0.40}$ junctions exhibiting reach fine structure with a prominent peak at 1.7 mV, a small local

maximum on a steep slope at 1.0 mV, and a distinct dip at 3.8 mV shown by related arrows. An analysis of the measured data based on a complex inner-gap structure in transport characteristics of superconducting junctions with degraded interfaces [1.44] permitted to extract the values of the energy gaps Δ_s = 0.5 meV and Δ_l = 2.5 meV. The presence of the two superconducting gaps in the Mo-Re alloy probed by tunneling spectroscopy indicates that one of the most probable scenarios explaining the significant increase in T_c upon alloying Mo with Re may be interband interaction.

1.3 Amorphous versus crystalline superconductors: two structural extremes

Solids are characterized by a rigid structure of molecules, ions, or atoms arranged in an orderly or non-orderly manner. The major difference between crystalline (discussed above) and amorphous (to be discussed below) compounds lies just in the long-range structural order that can be always accurately defined by periodically translating unit cells. The lack of inherent periodicity with an appreciable degree of short-range and / or medium-range orders are distinct features of the amorphous phase.

Three-dimensional (3D) crystal is a solid material in which the constituents are organized in a highly ordered microscopic structure forming a lattice extending in all directions. The crystalline materials retain their original shape and consistency, their mechanical strength, thermal conductivity, refractive index, and electrical conductivity differ in diverse directions. Fast cooling such substances may lead to an amorphous structure with irregular geometrical shapes. For example, quartz is a hard crystalline mineral composed of silicon and oxygen atoms in a strict order, while it can turn into amorphous glass when cooled rapidly. Other examples of amorphous materials largely used due to their huge benefits and unique isotropic properties are rubber and polymers. Amorphous state has usually an internal structure comprising interconnected structural blocks that can be similar to the basic structural units in the corresponding crystalline phase of the same compound. Therefore, the type of a solid depends primarily on the connectivity between its elementary building blocks, namely, crystals are characterized by a high degree of connectivity while the structural blocks in amorphous materials have lower connectivity.

As was indicated above, some elements that are poor superconductors in the crystalline phase (such as Ga and Bi) or do not exhibit superconductivity at all (as Be [1.66]) become superconductive in the amorphous state [1.67, 1.68]. Early work [1.67] explained such finding by the lack of a densely packed structure in the crystalline phase and promotion of superconductivity by effectively compacting it. Other elements, such as Pb, have densely packed structure and are good superconductors already in the crystalline phase, but in this case, the disorder, if it is introduced, only reduces the critical temperature of the superconducting transition. Unfortunately, such explanation turned out to be insufficient and understanding the effect of structural disorder on superconductivity remains a long-standing problem waiting for its solution, see the reviews [1.4, 1.69, 1.70].

Because of the lack of a theoretical framework able to describe, in a reductionism way, the effect of structural disorder as well as limited experimental characterization, amorphous materials are used quite rarely comparing to crystal counterparts. Nevertheless, there are some important fields as displays, solar cells, optical fibers, and others where non-crystalline samples found their niches. The most important amorphous thin-film application is a few nm thin SiO_2 layer serving as an isolator above the conducting channel of a metal-oxide semiconductor field-effect transistor. Also, in some cases, the transition between amorphous and crystalline phases determines the device operation, for example, in phase-change memory setups.

Main applications need thin solid films of a few nanometers to some tens of micrometers thickness deposited upon a substrate with the goal of forming amorphous phases. Necessary (but not sufficient) condition for their occurrence is that the deposition temperature must be below 30 % of the melting temperature (for higher values of the deposition temperature, the surface diffusion of deposited atoms would allow for the formation of crystallites with a long-range atomic order) [1.71]. Emergence of separate building blocks when the system is crossing a continuous phase transition in finite time can be explained by the formation of topological defects described by the Kibble-Zurek mechanism valid in the limit of slow quenches. This approach predicts an universal power-law scaling of the density with the quench time in which the transition is crossed. While Kibble-Zurek scaling holds below a critical quench rate, for

faster quenches, the defect density and the freeze-out time become independent of them, exhibiting universal power-law scaling with the final value of the control parameter. Such amorphous metallic layers played a decisive role in the discovery of superconductivity in amorphous metals.

Historically, two different paradigms concerning the structure of amorphous solids were formulated in the 1950s, namely, the rigid band approximation and the random network approach which evolved into a modern structural theory of amorphous solids [1.72]. The modern interpretation considers structurally similar building blocks connected in a network, where intermediate-range order, that is, order on a scale larger than that of the individual building blocks, may persist up to a certain extent. However, even now some fundamental questions remain without answers. What is the extent of intermediate and long-range orders in the amorphous structure or what is the amount of randomness in the system? Second, how close is the relationship between the fundamental building blocks in amorphous materials and the corresponding crystals? Ref. [1.73] showed that it is possible to quantify the extent of structural similarity between amorphous and crystalline phases, thus shedding light on a problem debated for more than half a century. The authors of this work argued that there is no definite answer, valid for all amorphous materials but individual systems can show a degree of similarity toward certain crystalline polymorphs, which is not necessarily limited to short-range order. For some amorphous systems, the network building units might be very similar to those of a crystalline polymorph, while other systems may show distorted network building units but with more intermediate-range order.

Due to the very short mean free path of electrons, amorphous materials provide a good model platform for analyzing the correlation between superconductivity and disorder [1.4]. The appearance of novel vortex phases in such samples was another subject of interest [1.74, 1.75]. Finally, the extraordinary phase homogeneity, little dependent on the crystal structure of the seed layer, has led to the fact that homogeneously disordered (amorphous) superconducting thin films are promising materials for use in superconducting micro- and nanoscale devices as superconducting detectors [1.76, 1.77] and vortex memory devices [1.78].

Below we will take as an example our results for silicon- and germanium-based amorphous superconducting films, α-MoGe and α-MoSi, with critical

temperatures T_c up to about 7.5 K, which have been previously used in high-performance integrated quantum photonic circuits (see the reviews [1.79–1.81] and references therein). Recent novel applications for α-MoGe and α-MoSi superconductors include quantum phase slip nanowire devices [1.82, 1.83], superconducting memory [1.84], hybrid superconductor-ferromagnet spin valves [1.85], *etc*. High normal-state resistivity and low superfluid density of amorphous superconductors can be exploited for the design of SQUIDs with tunable characteristics [1.86] as well as may be useful for building protected qubits [1.87].

Below we present our point-contact data for a MoSi thin layer stabilized in an amorphous phase and main characteristics of α-MoGe based Josephson junctions, which were fabricated and studied for the first time in Ref. [1.88]. Concerning the α-MoSi-Ag point contacts, we have followed the methodology described above. Measuring differential conductance–versus–voltage characteristics and comparing them with theoretical expectations [1.61] we have found the energy gap value equal to 0.35 meV, see Fig. 1.8.

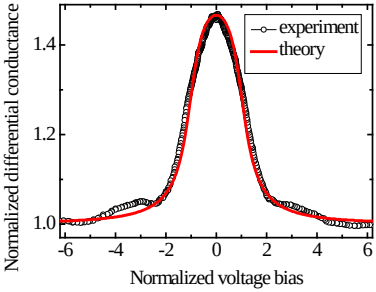

Fig. 1.8 – Normalized differential conductance $G(V)R_N$ versus normalized voltage bias eV/Δ characteristic measured for a representative point-contact sample formed by a silver tip and an amorphous α-MoSi sample (dots) compared with a fitting curve (solid line). The energy gap Δ = 1.18 meV, the effective interface scattering parameter Z = 0.11 meV, the Dynes parameter Γ = 0.28 meV, the normal-state resistance R_N = 17.2 Ohm

Our next step was the fabrication of Josephson junctions based on amorphous superconducting films [1.88]. Up to now, the main technological approach in this field remains the whole-wafer Nb/Al/AlO_x/Nb trilayer process [1.89], when the junctions are fabricated *in situ* and the tunnel barrier is formed by thermal oxidation of an Al overlayer deposited on the bottom Nb

layer. The barrier transparency in such trilayer is mainly controlled by the oxygen exposure, the product of oxygen pressure and oxidation time [1.90]. An advantage of the Nb/Al methodology is that it yields junctions with uniform properties over a large wafer area and good reproducibility from one fabrication batch to another. A standard deviation of the mean resistance values for a 5 mm × 5 mm test chip of 1 μm junctions is currently about 1 % [1.91]. This means that superconducting circuits have already reached the density of very large-scale integration, previously achieved only by semiconductor technology.

In spite of this progress, further improvement in the Josephson-junction tunneling quality remains an important task. In particular, this can be attained by reducing the Al overlayer thickness. At the same time, the drawback of the Nb/Al/AlO_x/Nb technology is that thin Nb films are granular. Then an unoxidized part of the Al overlayer tends to diffuse through the grain boundaries inside the Nb film [1.92] leading to degradation of the junction quality, especially in high-transparency junctions [1.93], and the need to use rather thick overlayers [1.94]. The solution to this problem can be the use of amorphous superconducting electrodes instead Nb ones. In the paper [1.88], related technique for obtaining such trilayer setups was described in detail. Obtained in such way sandwich-type Josephson tunnel junctions with α-MoGe electrodes demonstrated the potential of the technology for superconducting electronics.

The Josephson multilayers were deposited *in situ* on oxidized Si substrates at room temperature using DC magnetron sputtering from $Mo_{75}Ge_{25}$ and Al targets while the tunnel barrier was formed by thermal oxidation of an Al overlayer exploiting the well-known ability of aluminum to form spontaneously a self-healing surface oxide. For some devices, a thin (1.3 nm) Al layer was deposited on top of the bottom oxidized Al overlayer prior to the deposition of a top MoGe layer. It is known that such procedure can considerably improve the tunneling quality of the junctions, specifically, the characteristic voltage. The superconducting transition temperature T_c of the α-MoGe films was in the range of 6.5 K to 7.0 K, the surface roughness of a typical 160 nm thick α-MoGe layer used for the junction fabrication was 0.27 nm. For comparison, the surface roughness of a 120-nm thick Nb film, used as a base electrode in Nb/Al/AlO_x/Nb junctions, was 0.66 nm [1.88]. Therefore, in

amorphous films, the surface uniformity was better than that in Nb counterparts, see Fig. 1.9.

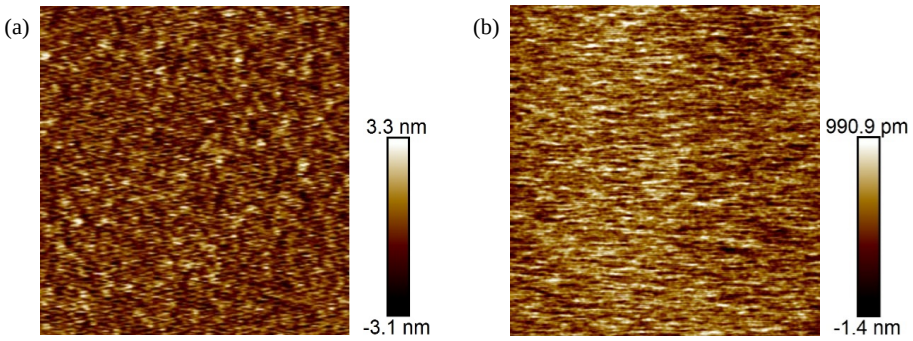

Fig. 1.9 – AFM images of a 120 nm thick Nb film (a) and 160 nm thick MoGe film (b) deposited onto oxidized Si substrates at room temperature. In both cases, the scanned area was 1.5 μm × 1.5 μm. Adapted from Fig. 1 in Ref. [1.88]

Below we present main results obtained for one of two types of devices studied in Ref. [1.88], namely, MoGe(160)/Al/AlO_x/(1.3)/Al(1.3)MoGe(80) where the numbers in parentheses are thicknesses of respective films in nm (that after Al/AlO_x is the initial thickness of the Al overlayer before oxidation). The oxidation exposure dose was 31 mTor × min. Josephson devices with lateral dimensions of 10 μm × 10 μm and 5 μm × 5 μm were formed using optical lithography and reactive ion etching, They were characterized in a liquid He transport Dewar for measurements at 4.2 K, and in a Quantum Design MPMS cryostat at various temperatures. Typical current-voltage characteristics (*I*–*V* curves) are shown in Fig. 1.10. For comparison, we demonstrate also typical *I*–*V* curve taken at 4.2 K for a Nb(120)/Al/AlO_x/(8.4)/Al(1.3)Nb(70) junction that was fabricated with an oxidation dosage of 326 mTorr × min. Let us turn attention to the fact that in the Nb-based junctions, a considerably thicker Al overlayer was needed for obtaining appreciable tunneling quality.

Notice also that, even at lower oxidation dosages, resistance of the MoGe-based junctions is much higher than that in Nb-based junctions. For example, the resistance of the Nb/Al/AlO_x/Al/Nb junction fabricated with ten times the oxidation dosage (its *I*–*V* characteristic is shown in Fig. 1.10 as an inset) has almost half the resistance of the MoGe junction (the main panel in Fig. 1.10).

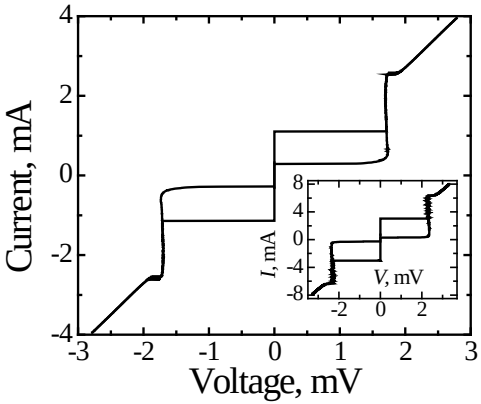

Fig. 1.10 – Main panel: Typical current-voltage characteristic of the MoGe(160)/Al/AlO_x/(1.3)/Al(1.3)MoGe(80) junction. Inset: *I*–*V* curve for a Nb(120)/Al/AlO_x/(8.4)/Al(1.3)Nb(70) junction. Critical temperature of the MoGe films was 7.0 K, the temperature of the transport measurements was 4.2 K. Adapted from Fig. 3 in Ref. [1.88]

The 'knee' structure seen slightly above the sum of the two energy gaps indicates the presence of an underoxidized aluminum interlayer between Nb and AlO_x in the heterostructure and is the result of the proximity effect [1.95, 1.96]. It was obtained that the relative standard deviation of the 4.2 K resistance at 3 mV for seven Nb-based junctions on the same substrate was 0.008, which is slightly larger than that for the MoGe junctions. For the same thin Al overlayer in Nb junctions as in MoGe junctions, the spread of the junction resistances would be considerably larger. This is an indirect evidence that the uniformity of the tunnel barrier in the MoGe junctions surpasses that in Nb-based junctions. The latter statement is supported by recent progress in apprehending the process of the Al surface oxidation that was previously poorly understood [1.97–1.100]. Nguyen *et al*. [1.97] studied the mechanism of aluminum oxide formation using atomic resolution imaging in an environmental transmission electron microscope. The authors found that the oxidation occurs via island growth and proceeds atomic layer-by-layer into the aluminum. After sufficient time, a continuous ~1.5 nm thick semi-crystalline layer of the oxide covers the surface up to the saturation thickness, depending on the oxygen pressure (higher pressures result in faster initial oxidation rates and higher

critical oxide thicknesses) [1.99]. The aluminum oxide phase has been identified in many previous studies as spinel (γ) Al_2O_3 oxide which is known to exhibit large structural differences due to variations in stoichiometry, temperature, pressure, and film thickness, see Ref. [1.97] and references therein. The fully thickened film is amorphous and shows no long-range crystallinity [1.97]. These experimental findings were confirmed by fully *ab-initio* simulations [1.98] aimed at understanding the thermodynamic driving force behind the initial choice to grow in an amorphous phase or a crystalline phase (either the corundum (α) or spinel (γ) structures) for the aluminum oxide surface layer growing on a crystalline Al substrate.

For the Josephson multilayered junctions with higher barrier transparency comparing to that shown in Fig. 1.10, the temperature effect on the current-voltage characteristics was studied in the range of temperatures from 2.6 K to the critical value T_c about 7.0 K [1.88]. A set of current-voltage characteristics for a representative device, at 2.6, 3.0, 4.0, 4.5, 5.0, 5.5, 6.0, and 6.5 K, is shown in Fig. 1.11. In these measurements, magnetic fields of 120–160 G were applied to suppress the Josephson current. The product of the junction resistance in the normal state R_N = 0.6 Ohm, and the subgap current $I^*(V^*)$ at the voltage bias $V^* = \Delta/e$, where Δ is an *apparent* energy gap, is shown in Fig. 1.12 as a function of temperature for three nominally identical junctions (scattered plots).

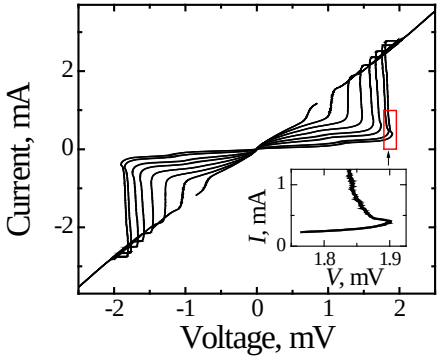

Fig. 1.11 – Main panel: A set of current-voltage characteristics for a MoGe(160)/Al/AlO_x/(1.3)/Al(1.3)MoGe(80) junction measured at 2.6, 3.0, 4.0, 4.5, 5.0, 5.5, 6.0, and 6.5 K. Magnetic field of 120–160 G was applied to suppress the Josephson current. The arrow shows a step associated with the flux flow. Inset: zoomed-in portion of the *I-V* curve for 2.6 K, marked by a red rectangle. Adapted from Fig. 4 in Ref. [1.88]

The subgap current vs temperature dependence presents further confirmation of high quality tunnel barriers in the Josephson junctions discussed. Fig. 1.11 exhibits a rapid decrease of the subgap current as the temperature goes down. For the curves measured at 6.0 and 6.5 K, the applied magnetic field was 160 G. However, even in such a field, the DC component of the AC Josephson current was not completely suppressed at voltage biases above that indicated by the vertical arrow. The Josephson current manifests itself as a smeared step, whose voltage position depends on the field. This step should not be confused with the step related to the subharmonic energy gap structure that is usually associated with the multiple Andreev reflections. Fig. 1.12 demonstrates the temperature dependence of the product I^*R_N as explained above. Current-voltage curves were calculated using the standard expression for the tunnel current between two identical superconductors: [1.101, 1.102]:

$$I(V,T)R_N = \frac{1}{e}\int_{-\infty}^{\infty} d\varepsilon N_s(\varepsilon - eV,T)N_s(\varepsilon,T)[f(\varepsilon - eV,T) - f(\varepsilon,T)], \qquad (1.5)$$

where $N_s(\varepsilon,T) = \mathrm{Re}\left\{\varepsilon / \sqrt{\varepsilon^2 - \Delta^2(T)}\right\}$ (1.4) is the normalized density of states in the superconducting electrode (the energy ε is measured from the Fermi level), $f(\varepsilon,T)$ is the Fermi distribution function, and $\Delta(T)$ was assumed to follow the conventional BCS dependence. Zero-temperature energy gap $\Delta_0 \equiv \Delta(0) =$ 1.14 meV was found from the same BCS curve using the values $\Delta(4.2\ \mathrm{K}) =$ 1.03 meV and $T_c = 7$ K. Note that the obtained ratio $2\Delta_0/k_BT_c =$ 3.77 is in agreement with that found by Tashiro *et al.* [1.103]. It is slightly larger than the BCS weak-coupling limit $2\Delta_0/k_BT_c = 3.52$ indicating moderate electron-phonon coupling in the amorphous α-MoGe superconductor.

In Fig. 1.11, one can see also a backward trend in the current-voltage characteristiucs at the gap-sum voltage, especially pronounced at lower temperatures. For example, the inset in Fig. 1.11 shows on a magnified scale a segment of the *I–V* curve near the voltage bias of $2\Delta/e$ outlined by the red dashed rectangle in the main panel for the curve measured at 2.57 K. A similar feature has been observed previously in a number of experiments involving tunnel junctions made of different superconducting materials and was associated with the gap suppression and formation of a nonequilibrium inhomogeneous state in superconducting films due to self-injection of quasiparticles [1.104].

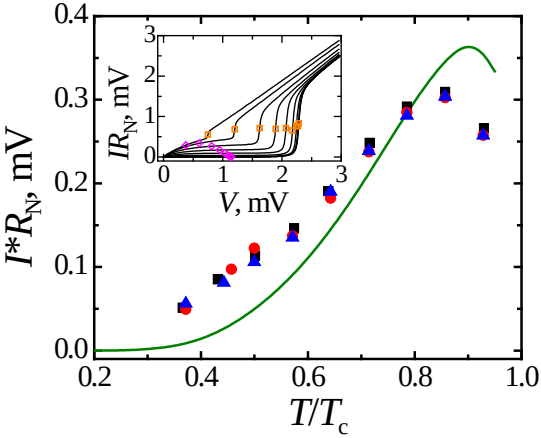

Fig. 1.12 – Main panel: Temperature dependence of the product I^*R_N, where the current I^* is measured at a voltage bias of $\Delta(T)/e$ ($\Delta(T)$ is an *apparent* energy gap) for three nominally identical MoGe(160)/Al/AlO_x/(1.3)/Al(1.3)MoGe(80) junctions (scattered plots). The solid line shows the theoretical dependence for an ideal tunnel junction with the same resistance as that of the measured junctions and $\Delta(0) = 1.14$ meV for both electrodes. Inset: a set of current-voltage characteristics calculated for an ideal tunnel junction at $T/T_c =$ 0.95, 0.9, 0.8, 0.7, 0.6, 0.5, 0.4, 0.3, 0.2, and 0.1 (curves from left to right, respectively). Orange squares denote voltages corresponding to $2\Delta(T)$. Magenta diamonds indicate current levels I^* corresponding to $\Delta(T)/e$ used for calculating the curve theoretically expected in the main panel. Adapted from Fig. 5 in Ref. 1.88

Since the effect of the gap suppression due to the excess quasiparticles, N_{exc}, created by the injection rate, I_0, may be important in some applications [1.105, 1.106], we have to analyze this feature in more detail. In the simplest case, $N_{exc} \equiv N(I_0) - N_T = I_0 \tau_\varepsilon$, where N_T is the thermal-equilibrium number density of quasiparticle excitations, the injection rate I_0 is the number of quasiparticles injected into a unit volume per second, and τ_ε is the quasiparticle relaxation time [1.107]. Let us now compare the impact of the same I_0 on the energy gap suppression $\delta\Delta$ in Nb and amorphous MoGe electrodes. In a nonequilibrium state, when the distribution function of excess quasielectron excitations $n_{exc}(\varepsilon) \neq 0$, the gap Δ can differ from its thermodynamic value Δ_0. For the "narrow" distribution function $n_{exc}(\varepsilon)$ in the S film ($\Delta \leq \varepsilon \leq \Delta + \delta\Delta$; $\delta\Delta << \Delta$), we get the following relation for a relative gap suppression $\eta_\Delta(n) \equiv [\Delta(0) - \Delta(n)]/\Delta(0)$ in a conventional BCS superconductor [1.108]:

$$\eta_\Delta(n) \approx 2\bar{n} = \int_\Delta^{\omega_D} \frac{2\varepsilon n_{exc}(\varepsilon)}{\Delta\sqrt{\varepsilon^2 - \Delta^2}} d\varepsilon, \tag{1.6}$$

where ω_D is the Debye energy. The excess quasiparticle concentration $\bar{n}$ is proportional to the ratio of $N_{exc}/N(0)$ where $N(0)$ is the single-spin density of states at the Fermi level [1.107].

Therefore, we can compare the effect of the same injection intensity I_0 in α-MoGe and Nb as follows:

$$\frac{\eta_\Delta^{MoGe}}{\eta_\Delta^{Nb}} \cong \frac{\tau_\varepsilon^{MoGe} N^{Nb}(0)}{\tau_\varepsilon^{Nb} N^{MoGe}(0)}. \tag{1.7}$$

The quasiparticle relaxation times τ_ε^{MoGe} and τ_ε^{Nb} depend on several factors such as the energy of excess quasiparticles, temperature, device size, environment, *etc*., hence it is difficult to precisely estimate this ratio. However, the data [1.109] indicate that the relaxation processes in MoGe are as fast as in Nb. Specifically, the recombination time is $\tau_r = 3.5 \cdot 10^{-11}$ s for MoGe [1.109], whereas for Nb at $T/T_c \approx 0.5$ and for the quasiparticle energy $\varepsilon = 2\Delta$, τ_r is about $9 \cdot 10^{-11}$ s [1.110]. In realistic experimental situations, in addition to the recombination, other processes, such as electron-phonon interactions, are involved in the quasiparticle relaxation. Liang and Kunchur [1.109] measured quasiparticle relaxation time τ_ε in MoGe films. At $T/T_c \approx 0.6$ (which corresponds to our experimental situation), one can infer $\tau_\varepsilon^{MoGe} \approx 7 \cdot 10^{-10}$ s from the data [1.109] while for Nb the energy relaxation time $\tau_\varepsilon^{Nb} \approx 3 \cdot 10^{-11}$ s [1.111]. Note that according to [1.104], the quasiparticle energy relaxation and gap relaxation times coincide.

Using the latter data and the densities of states at $\varepsilon = 0$, $N^{MoGe}(0) = 6.4 \cdot 10^{21}$ eV^{-1}cm^{-3} [1.112] and $N^{Nb}(0) = 9 \cdot 10^{22}$ eV^{-1}cm^{-3} [1.113], we obtain from Eq. (1.7) that the ratio $\eta_\Delta^{MoGe}/\eta_\Delta^{Nb} > 300$ for *the same* injection rate I_0. This estimate indicates that a nonequilibrium quasiparticle population is much easier to realize in MoGe films than in Nb films. The data in Fig. 1.11 are consistent with the conclusion.

Fig. 1.13 exhibits experimental dependencies of the critical current I_c versus magnetic field H applied parallel to the layers of 5 μm × 5 μm

Josephson junctions with higher critical current density j_c = 1.25 kA/cm^2. The $I_c(H)$ characteristic of a representative device, recorded at 4.2 K, is close to the theoretical expectation described by the relation $I_c|\sin(\pi\Phi/\Phi_0)/\pi\Phi/\Phi_0|$ (solid red line), where Φ is the magnetic flux penetrating the junction, and Φ_0=2.07·10^{-7} G·cm^2 is the flux quantum. A small deviation of the experimental $I_c(H)$ curve from theoretical one (in particular, a small asymmetry) is likely due to self-field effects and / or trapped flux [1.114, 1.115].

At the beginning of this subsection, we have mentioned ('strange' from the first insight) behavior of superconducting characteristics in amorphous metal alloys, also known as metallic glasses. Good superconductors change little by introducing disorder into them while those with relatively small T_c's can sharply raise their superconducting transition temperature. It is important that at low temperatures, many disordered materials have properties very similar to each other, including specific heat and thermal conductivity. Additionally, these properties differ significantly from those of related ordered crystals. Both features can be observed analyzing relaxation processes in glass-forming materials that usually occur as a two-stage process. First, there is a fast or 'β-relaxation' process, having a weakly temperature-dependent relaxation time (usually on the order of picoseconds), followed by the primary or 'α-relaxation' process with a relaxation time ranging from picoseconds to even minutes [1.116].

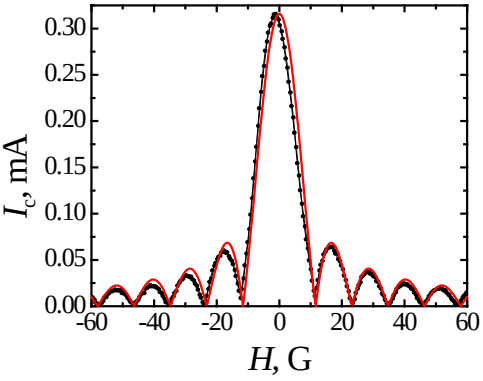

Fig. 1.13 – Ic vs H dependence of a 5 μm × 5 μm MoGe(160)/Al/AlOx/(1.3)/Al(1.3)MoGe(80) junctions at 4.2 K (black line + symbol plot). Red solid line is a theoretical dependence calculated using the period of the diffraction pattern δH = 11.6 G. Adapted from Fig. 6 in Ref. [1.88]

Furthermore, at a certain frequency range, amorphous materials exhibit excess of soft vibrational modes comparing to crystals, known as a 'boson peak' [1.117, 1.118], which shows up in the vibrational density of states $F(\omega)$ upon normalizing it by the Debye law ω^{d-1}: $F(\omega)/\omega^{d-1}$ (here d is the spatial dimensionality and ω is the angular frequency). Notice that $F(\omega)/\omega^{d-1}$ = const in the Debye's theory for crystals that successfully explained thermal behavior of ordered solids but cannot be straightforwardly applied to amorphous ones due to structural disorder and the absence of translational order, making it extremely challenging task.

The authors of Ref. [1.118] used sophisticated molecular dynamics computer simulations for revealing microscopic origins of the boson peak through numerical investigations of the dynamic structure factor of two-dimensional model glasses over a wide frequency–wavenumber range. They found that quasi-localized vibrations of string-like dynamical defects inside the material can move together, thus being important drivers of the anomalous observations in glassy systems: the boson peak, fast β-relaxation and slow structural relaxation. This conclusion has many important implications for both basic science and practical applications.

Typically, superconductivity in amorphous materials is strongly coupled, with the electron-phonon coupling parameter $\lambda > 1$ and the superconducting gap much larger than the BCS prediction, Presence of the boson peak means the need to transit from the oversimplified Bardeen-Cooper-Schrieffer model to the Eliashberg theory of strong-coupling phonon-mediated superconductivity [1.58, 1.119, 1.120]. This theory considers phonons as ballistic excitations while the largest part of the vibrational density of states for an amorphous material is formed by phonons, which propagate diffusively due to intense scattering promoted by disorder. Their Green's function

$$G_{\lambda}(\omega,k)=\frac{1}{\omega^{2}-\Omega_{\lambda}^{2}(k)+i\omega\Gamma_{\lambda}(k)}, \tag{1.8}$$

takes into account propagating and diffusive damping (due to disorder-induced scattering) terms given by $\Omega_{\lambda}^{2}=v_{\lambda}^{2}k^{2}$ and $\Gamma_{\lambda}(k)=D_{\lambda}k^{2}$. Here v_{λ} and D_{λ} are the (dressed) speed of phonon propagation and the diffusion constant of the λ phonon branch, respectively, the subscript λ refers to either

longitudinal λ = L or transverse λ = T displacement fields, the diffusive form D_λ of the damping follows from related simulations performed over a broad range of k, see the references in Ref. [1.121]. Respectively, the Eliashberg electron-phonon interaction function equals to

$$\alpha^2 F(\vec{k},\vec{k}',\omega) \equiv N(\mu)\left|g_{\vec{k},\vec{k}'}\right|^2 B(\vec{k}-\vec{k}',\omega) \tag{1.9}$$

with the electronic density of states $N(\mu)$ at the chemical potential μ, the electron-boson matrix element $g_{\vec{k},\vec{k}'}$, and the spectral function

$$B_\lambda(\omega,k) = -\frac{1}{\pi}\operatorname{Im} G_\lambda(k,\omega+i\delta) \tag{1.10}$$

Using Eq. (1.8) we obtain [1.121]

$$B(\omega,k) = \frac{\omega\Gamma(k)}{\pi\left\{\left[\omega^2-\Omega^2(k)\right]^2+\omega^2\Gamma^2(k)\right\}} \tag{1.11}$$

Next, the Fermi-surface-averaged spectral function

$$\alpha^2 F(\omega) = \frac{1}{N(\mu)^2}\sum_{\vec{k},\vec{k}'}\alpha^2 F(\vec{k},\vec{k}',\omega)\delta(\varepsilon_{\vec{k}}-\mu)\delta(\varepsilon_{\vec{k}'}-\mu) \tag{1.12}$$

can be used for calculations of basic superconducting parameters as it was shown for crystalline samples in Ref. [1.58].

Using the Lorenzian form (1.11) to model the phonon spectral density, the authors of Ref. [1.121] went to some very important conclusions. First, they obtained (known from experiments) linear in frequency behavior of the Eliashberg function $\alpha^2F(\omega)$ in the low-ω limit. Second, they found a non-monotonic dependence of the electron-phonon coupling parameter λ upon the disorder characteristic D (Fig. 1.14) with a maximum as a function of disorder, which monotonically grows upon increasing the speed of sound. Such tendency may be ascribed to two competing factors. On the one hand, the Lorentzian vibrational peak becomes bigger, which makes more phonon states accessible for pairing at low ω. On the other hand, upon increasing D further, the Lorentzian becomes broader and eventually shallower due to the term $\sim D^2$ in the denominator of the Lorentzian (1.11). These two opposite tendencies cause the presence of a peak in the dependence of λ on the diffusivity D., the position

of which shifts towards higher diffusion coefficients as the transverse speed of sound in a given material increases (a dashed line in Fig. 1.14) [1.121].

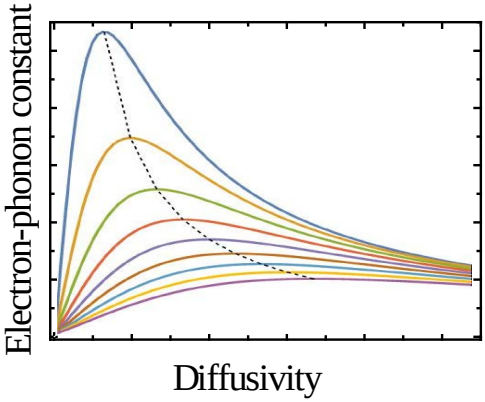

Fig. 1.14 – Schematic illustration of the electron-phonon coupling constant λ on the diffusivity D of transverse vibrational excitations for various values of the transverse speed of sound. The dashed line demonstrates an increase of the maximum position towards higher diffusion coefficients with increasing the speed of sound. The units for both axes are arbitrary. Adapted from Fig. 2 in Ref. [1.121]

The presence of a maximum in the λ-vs-D dependence shown in Fig. 1.14 means that the disorder effect on the main superconducting characteristics of a particular metal is controlled by its position on the λ-vs-D curve in the original crystalline state. If the initial superconductor has a relatively small value λ, then the disordering could enhance the electron-phonon coupling strength and we may observe the growth of T_c, as it happens, for example, in aluminum [1.122]. If, however, we are dealing with a superconductor with a sufficiently large λ, as in lead, then converting it to an amorphous state or adding impurities, most likely, will not lead to any noticeable effect or even cause slight weakening of the electron-phonon interaction.

These conclusions are well supported by comparing related experimental data for two model materials, for which the structural disorder can be varied continuously from the pure crystalline material limit (zero disorder) to the amorphous state (strong disorder) whether by means of alloying or by creating amorphous samples. Reconstructed Eliashberg functions feature two distinct peaks corresponding to transverse T (low frequency) and longitudinal L (high frequency) vibrational excitations. It is evident that, upon increasing the

degree of disorder, both peaks become much broader due to the increase of the phonons diffusivities D_T and D_L. This impact is more pronounced in the low-frequency region in agreement with the boson peak effect. Fig. 1.15 shows that in spite of the greater changes in the Eliashberg functions of Pb and related alloys in the low-frequency region, the disorder effect on T_c is much stronger in Al than in Pb, since, firstly, the crystalline aluminum has a significantly lower electron-phonon interaction strength, and secondly, due to the stronger broadening effect for longitudinal phonons.

The latter statement was also supported by experiments on nanostructured samples of Sn, a weekly coupled superconductor [1.26]. Relating their results to the bulk Sn phonon density of states, the authors [1.26] pointed out on a slightly increased number of low-energy phonon modes and a strong decrease in the number of high-energy phonon modes. It is important to note principal difference between Sn and Nb_3Sn thin films [1.122]. In Nb_3Sn, a strong coupling superconductor, with decreasing film thickness, a slight decrease in T_c was observed that was mainly caused by an electron confinement factor rather than phonon softening. Again, as in the case of Pb and Al discussed above, this difference arises due to lower electron-phonon interaction strength in the initial material.

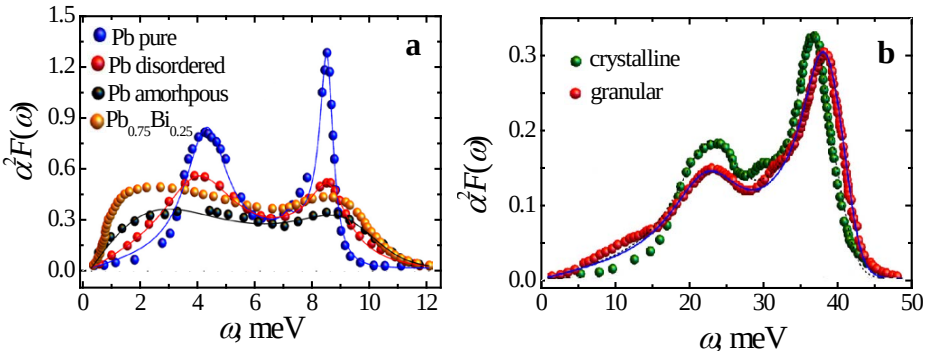

Fig. 1.15 – Eliashberg electron-phonon interaction functions α2F(ω) for Pb and PbBi alloy [1.123, 1.124] (a) and Al [100] (b) reconstructed from tunneling experiments [1.123, 1.124] and [1.125], respectively. Adapted from Figs. 3 and 5 in Ref. [1.121]

1.4 Superconducting quasicrystals and high-entropy alloys: intermediate compounds between crystalline and amorphous solids

We have discussed above two extreme states – crystalline and amorphous superconductors. According to the conventional crystallography, a crystal as a periodic arrangement of atoms with translational periodicity, leading to an infinitely extended crystal structure by aligning building blocks called unit cells [1.126]. The discovery of quasicrystals, stable solid-state materials without translational symmetry but having a high degree of order in their atomic arrangement (as manifested in the occurrence of sharp diffraction spots) led to a paradigm shift in materials science. Another feature that significantly distinguishes them from traditional crystals is the presence of a non-crystallographic rotational symmetry as fivefold symmetry in icosahedral quasicrystals. It was found that these specifically ordered materials exhibit anomalous electronic properties [1.127, 1.128], quantum criticality [1.129], etc. Superconductivity that emerged below T_c = 50 mK was observed for the first time in 2018 in an Al-Zn-Mg alloy [1.126]. In fact, it was the first quasicrystal exhibiting electronic long-range order. The authors revealed no difference between their samples and conventional weak-coupling superconductors. Nevertheless, during the last years the nature of superconductivity in such exotic materials has become the subject of intense theoretical debate, see Ref. [1.130] and references therein. In particular, the authors of Ref. [1.131] drew attention to the difference between the BCS theory and experiment [1.126] concerning the jump in the specific heat at the superconducting transition and explained it considering the attractive Hubbard model on the Penrose tiling as a simple theoretical model. However, from a theoretical point of view, there is no reason to believe that the mechanism of superconductivity in quasicrystals is fundamentally different from that in the BCS theory [1.130]. Undoubtedly, a further more detailed study of superconductivity in quasicrystals is needed.

Let us move on to more studied substances that also occupy an intermediate position between crystalline and amorphous superconductors, namely, to high-entropy alloys (HEA), a novel class of single-phase crystals with random solid solutions of five or more elements of a nearly equal composition [1.132]. These materials received a great amount of attention in recent years because

of their multi-elemental composition providing not only an enormous number of combinations for materials discovery but also a unique microstructure for property optimization [1.132, 1.133]. In particular, HEAs are known to exhibit intriguing electronic properties and superior mechanical properties such as a combination of high yield strength and ductility, high strength at high temperatures, strong resistance to corrosion and oxidation, outstanding thermal stability and so on, which are primarily derived from the high atomic disorder and near-equiatomic (5–35 at. %) mixing of different elements. The concept of this type of materials was originally proposed for simple crystal structures such as face-centered-cubic (fcc), body-centered-cubic (bcc), and hexagonal-closed packing (hcp) structures, all of which possess only one crystallographic site. Now this idea was implemented in many multi-site alloys beyond the structures mentioned above. Up to now there was not proposed a strict definition of HEAs. One of the definitions of HEA is that more than five elements with an atomic fraction of each element between 5 % and 35 % randomly occupy one crystallographic site [1.134]. The other definition uses the value of mixing entropy ΔS_{mix}, which is expressed as follows:

$$\Delta S_{\text{mix}} = -R\sum_{i=1}^{n} c_i \ln c_i \,, \tag{1.13}$$

where n is the number of components, c_i is the atomic fraction and R is the gas constant. According to this equation, we classify low-entropy alloys as having an R value less than 0.69, medium-entropy alloys as having an R value between 0.69 and 1.60, and HEAs has having an R value of 1.60 or larger [1.135].

One of the attractive properties of HEAs is superconductivity [1.136, 1.137, 1.138]. In 2014, Koželj *et al.* reported the synthesis of the first HEA superconductor $Ta_{0.34}Nb_{0.33}Hf_{0.8}Zr_{0.14}Ti_{0.11}$ with T_c = 7.3 K [1.37]. It was a type II superconductivity with the upper critical field $H_{c2}(0)$ = 82 kOe. The measured physical properties were consistent with a conventional phonon-mediated superconductivity in the weak electron–phonon coupling limit. One of the salient features of this superconductor is that it exhibits extremely stable superconductivity under pressures up to 190 GPa. Later on, superconductivity was also observed in other HEAs, in particular, in CsCl-type Sc-Zr-Nb-Rh-Pd

and Sc-Zr-Nb-Ta-Rh-Pd alloys [1.139] and *Tr*Zr_2-type (Fe,Co,Ni,Rh,Ir)Zr_2 [1.140, 1.141]. Most interestingly, the superconducting $(ScZrNb)_{0.65}[RhPd]_{0.35}$ compound has $T_c \approx 9.7$ K and $H_{c2} \approx 100.7$ kOe, comparable to those characteristics of NbTi alloys [1.142]. From the basic viewpoint, HEA superconductors composed of transition metals can be regarded as an intermediate state between crystalline and amorphous materials, that is why their study is expected to shed light on the relationship between main parameters and the structural properties of superconductors.

Such an analysis based on experiments carried out on the Ta-Nb-Hf-Zr-Ti system, the most explored combination, was made by the authors of Ref. [1.137]. In particular, a large amount of data already available was considered from the perspective of an empirical Matthias rule [1.143] for T_c plotted as a function of the valence electron count per atom (VEC), see also the review [1.144]. This rule states that the superconducting critical temperature of transition-metal crystalline superconductors vs VEC dependence has the form of broad peak structures at specified VEC values. Indeed, in the compound $(TaNb)_{1-x}(HfZrTi)_x$ ($0.2 \leq x \leq 0.84$) where, depending on x, T_c ranges from 4.5 K to 8.0 K the maximum T_c is reached at the VEC value about 4.7 following the Matthias rule for crystalline transition-metal superconductors [1.145]. The curve of the VEC dependence of T_c for the HEAs lies between those of crystalline 4*d* metal solid solutions and amorphous 4*d* metals.

One of the high-impact results is the superconducting properties under high pressures. The $(TaNb)_{0.67}(HfZrTi)_{0.33}$ HEA superconductor showed a robust zero-resistance state up to 190.6 GPa [1.146]. This observation makes the HEAs promising candidates for superconducting materials working under extreme conditions. Another important conclusion to be noticed is the thermal annealing effect [1.147]. Long-term annealing induces short-range clustering of atoms, modifying the HEA microstructure. However, the superconducting properties are rather insensitive to such changes. There were reported first successful fabrications of $(TaNb)_{1-x}(HfZrTi)_x$ thin films using a magnetron sputtering method [1.148]. The highest $T_c = 6.8$ K was observed at $x = 0.43$ with VEC = 4.57. It was also found that the high-entropy state tends to stabilize the crystalline structure in spite of a rather large mismatch of atomic radii among constituent elements and therefore the high-entropy impact on

superconducting characteristics is correlated more to the structural properties than the electronic ones.

Let us now compare our results for Mo-Re crystalline alloys presented above with HEA compounds which are including molybdenum and rhenium as constituent elements. Ref. [1.149] reported related data for several hcp HEA superconductors based on a Mo-Re-Ru hcp alloy with the critical temperature T_c of 9.1 K. The highest T_c of 4.7 K was observed for a $Mo_{0.225}Re_{0.225}Ru_{0.225}Rh_{0.225}Ti_{0.1}$ compound. We can see that the superconducting transition temperature does not reach values typical for binary Mo-Re crystalline samples. This again indicates that the main benefit of the HEA samples is not their superconducting parameters but other superior properties arising due to high mixing entropy.

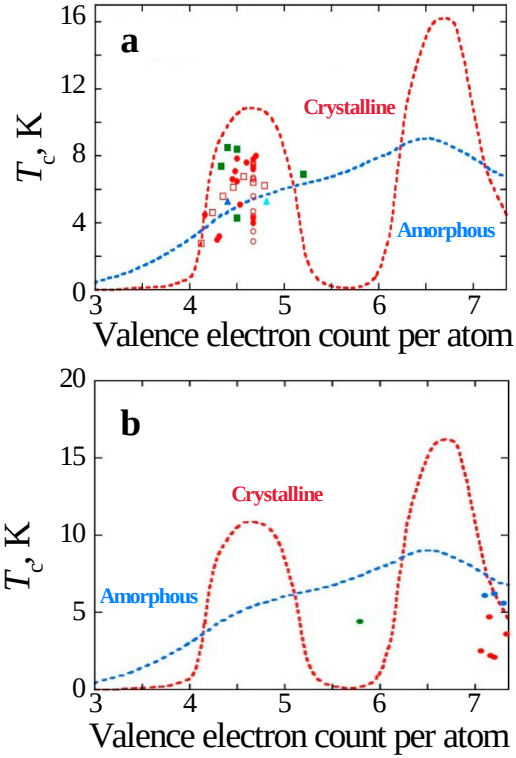

Fig. 1.16 – Superconducting transition temperatures Tc vs valence electron count per atom (VEC) dependence for bcc (left) and hcp and hcp-related (right) HEA superconductors compared with related dependences for crystalline 4d metal solid solutions and amorphous 4d metal superconductors. Adapted from Figs. 3 and 5 in Ref. [1.137]

The elemental choice for superconducting HEA compounds is now limited by Hf, Zr, Ti, Ta, Nb, Mo, V, Re, Ru and Rh with a VEC between 4 and 5 for bcc materials and neat 7 for hcp and hcp-related alloys. Due to it, the total number of HEA superconductors is rather small. Such state of affairs opens up a wide field of machine learning activities [1.150, 1.151]. In this regard, the most important, although perhaps not feasible in practice, task is to find a high-T_c HEA. As was argued by the authors of the overview [1.137], interest in HEA superconductors will grow due to the high degree-of-freedom of the HEA design. For example, it can relate HEA superconductors containing magnetic element(s) [1.137], eutectic [1.152], or gum-like [1.153] HEA superconducting compounds. In the first case, we may anticipate an exotic superconducting state originating from the large mixing entropy [1.137]. The change of the internal arrangement in eutectic HEAs could lead to the enhancement not only T_c but the critical current density as well since the microstructure of such material can be regarded as built-in multifilamentary one [1.137]. Gum metals. *i. e.*, metals which can be bent as gum [1.154] (for example, as-cast $Al_{0.05}Nb_{0.24}Ti_{0.4}V_{0.05}Zr_{0.26}$ [1.153]) are highly advantageous for making next-generation superconducting wires because their good superconducting properties are preserved even after cold rolling [1.137]. Last, the creation of new superconducting devices based on HEAs remains the most important task of this research line.

1.5 Conclusions

The interplay between disorder and superconductivity is a fascinating fundamental phenomenon in quantum physics. The famous Anderson's theorem states that conventional superconductors are insensitive to dilute nonmagnetic impurities. Even more, in the strong disorder regime far beyond the scope of the Anderson's theorem application, destruction of superconductivity and even superconductor–insulator transitions may take place [1.4]. That is why disorder-enhanced superconductivity is usually considered anomalous. However, our review shows that this effect is not so rare and manifests itself in a wide range of superconductors with different degrees of structural ordering. Notice that superconducting properties can be controlled not only by the overall density of impurities and / or defects but also by their spatial correlations [1.155].

To demonstrate the ubiquity of this phenomenon, we considered two limiting cases – a simplest binary alloy with a clear crystal structure (on the example of an alloy of molybdenum with rhenium) and an amorphous superconductor with a short-range ordering (on the example of *a*-MoSi and *a*-MoGe films). In the first case, a sharp increase in the critical temperature of the normal-to-superconducting transition was caused by modification of the electronic structure due to alloying, while in the second case, the main factor was the diffusive character of the phonon propagation promoted by increased number of scattering events. The best way to understand the interplay between the two sources of superconductivity enhancement would be careful and well-controlled study of an intermediate case, superconducting high-entropy alloys characterized by a multi-component alloy in which five or more elements are randomly occupying a crystallographic site. The materials research on the latter materials has just started recently, and we believe that it will bring new unexpected results. Solving the dilemma of crystalline and amorphous superconductors will give researchers a better understanding of chemical design principles for optimizing the key critical parameters in order to create novel superconductor-based devices.

This work was partly supported by the German-Ukrainian collaborative project “Controllable quantum-information transfer in superconducting networks” (DFG project SE 664/21-1, No. 405579680). E.Zh. acknowledges financial support from Deutscher Akademischer Austauschdienst (DAAD) under the grant “Non-unitary quantum devices as p-bites for stochastic computing”, the funding programme 57552335. M.B. is grateful for the financial support from Volkswagen Stiftung under the grant 9B884 “Novel quantum platforms for cryogenic sensing and stochastic computing”.

1.6 References to chapter 1

1.1 Shalnikov A. Superconducting thin films. *Nature.* 1938. V. 142. P. 74.

1.2 Anderson P. W. Theory of dirty superconductors. *J. Phys. Chem. Solids.* 1959. V. 11. P. 26–30.

1.3 Abrikosov A. A., Gor’kov L. P. Superconducting alloys at finite temperatures. *J. Exp. Theor. Phys.* 1959. V. 38. P. 319–320.

1.4 Finkel'stein A. M. Suppression of superconductivity in homogeneously disordered systems. *Physica B*. 1994. V. 197. P. 636–648.
1.5 Fisher M. P. A. Quantum phase transitions in disordered two-dimensional superconductors. *Phys. Rev. Lett*. 1990. V. 65. P. 923–926.
1.6 Gupta A., Awana V., Samanta S., Kishan H., Narlikar A. Disordered superconductors. In: *Frontiers in Superconducting Materials*. Ed. By Narlikar A. V. Springer: Berlin, Heidelberg. 2009.
1.7 Alloul H., Bobroff J., Gabay M., Hirschfeld P. J. Defects in correlated metals and superconductors. *Rev. Mod. Phys.* 2009. V. 81. P. 45.
1.8 Sacépé B., Feigel'man M., Klapwijk T. M. Quantum breakdown of superconductivity in low-dimensional materials. *Nat. Phys*. 2020. V. 16. P. 734–746.
1.9 Petrović A. P., Ansermet D., Chernyshov D., Hoesch M., Salloum D., Gougeon P., Potel M., Boeri L., Panagopoulos C. A disorder-enhanced quasi-one-dimensional superconductor. *Nat. Commun.* 2016. V. 7. P. 1–10.
1.10 Lowe A., Kagalovsky V., Yurkevich I. V. Disorder-enhanced superconductivity in a quasi-one-dimensional strongly correlated system. *Phys. Rev. Res.* 2021. V. 3. P. 033059.
1.11 Zhao K., Lin H., Xiao X., Huang W., Yao W., Yan M., Xing Y., Zhang Q., Li Z.-X., Hoshino S., Wang J., Zhou S., Gu L., Bahramy M. S., Yao H., Nagaosa N., Xue Q.-K., Law K. T., Chen X., Ji S. H. Disorder-induced multifractal superconductivity in monolayer niobium dichalcogenides. *Nat. Phys.* 2019. V. 15. P. 904–910.
1.12 Leroux M., Mishra V., Ruff J. P., Claus H., Smylie M. P., Opagiste C., Rodie P., Kayani A., Gu G. D., Tranquada J. M., Kwok W.-K., Islam Z., Welp U. Disorder raises the critical temperature of a cuprate superconductor. *PNAS*. 2019. V. 116. P. 10691–10697.
1.13 Grassme R., Seidel P. The BCS Gap equation within the van Hove scenario of high-Tc superconductivity. *J. Supercond.* 1996. V. 9. P. 619–624.
1.14 Grassme R., Seidel P. An upper bound for the gap ratio of superconductors within the BCS theory for weak coupling. *Solid State Commun*. 1996. V. 98. P. 143–146.
1.15 Litak G. Van Hove singularity and superconductivity in a disordered Hubbard model. *Phys. Stat. Sol. B*. 2002. V. 229. P. 1427–1449.

1.16 Arnold G. B. Theory of thin proximity-effect sandwiches. II. Effects of s-wave elastic scattering. *Phys. Rev. B.* 1981. V. 23. P. 1171.
1.17 McMillan W. L. Tunneling model of the superconducting proximity effect. *Phys. Rev.* 1968. V. 175. P. 537.
1.18 Schopohl N., Scharnberg K. Tunneling density of states for the two-band model of superconductivity. *Solid State Commun.* 1977. V. 22. P. 371–374.
1.19 Golubov A. A., Mazin I. I. Effect of magnetic and nonmagnetic impurities on highly anisotropic superconductivity. *Phys. Rev. B.* 1997. V. 55. P. 15146.
1.20 Markowitz D., Kadanoff L. P. Effect of impurities upon critical temperature of anisotropic superconductors. *Phys. Rev.* 1963. V. 131. P. 563.
1.21 Belogolovskii M., Plecenik A., Grajcar M. Temperature effect on the quasiparticle spectrum of an impurity-doped superconductor with two separate electron groups. *Phys. Rev. B.* 2005. V. 72. P. 052508.
1.22 Mishra V. Effect of disorder on superconductivity in the presence of spin-density wave order. *Phys. Rev. B.* 2015. V. 91. P. 104501.
1.23 Bosworth D., Sahonta S. L., Hadfield R. H., Barber Z. H. Amorphous molybdenum silicon superconducting thin films. *AIP Adv.* 2015. V. 5. P. 087106.
1.24 Chen S. Z., Yang J. W., Peng T. Y., Chu Y. C., Yeh C. C., Hu I. F., Mhatre S., Lu Y.-J., Liang, C. T. Disorder-induced 2D superconductivity in a NbTiN film grown on Si by ultrahigh-vacuum magneton sputtering. *Supercond. Sci. Technol.* 2022. V. 35. P. 064003.
1.25 Scheurer M. S., Schmalian J. Topological superconductivity and unconventional pairing in oxide interfaces. *Nat. Commun.* 2015. V. 6. P. 1–10.
1.26 Houben K., Jochum J. K., Couet S., Menéndez E., Picot T., Hu M. Y., Zhao J. Y., Alp E. E., Vantomme A., Temst K., Van Bael M. J. The influence of phonon softening on the superconducting critical temperature of Sn nanostructures. *Sci. Rep.* 2020. V. 10. P. 5729.
1.27 Buckel W. Elektronenbeugungs-Aufnahmen von dünnen Metallschichten bei tiefen Temperaturen. *Z. Phys.* 1954. V. 138. P. 136–150.
1.28 Prakash O., Kumar A., Thamizhavel A., Ramakrishnan S. Evidence for bulk superconductivity in pure bismuth single crystals at ambient pressure. *Science*. 2017. V. 355. P. 52–55.

1.29 Bergmann G. Amorphous metals and their superconductivity. *Phys. Rep*. 1976. V. 27. P. 159–185.
1.30 Buzea C., Robbie K. Assembling the puzzle of superconducting elements: a review. *Supercond. Sci. Technol*. 2004. V. 18. P. R1.
1.31 Curzon A. E., Mascall A. J. Superconductivity in thin films of beryllium. *J. Phys. C.* 1969. V. 2. P. 382.
1.32 Gastiasoro M. N., Andersen B. M. Enhancing superconductivity by disorder. *Phys. Rev. B.* 2018. V. 98. P. 184510.
1.33 Gao M. C., Yeh J.-W., Liaw P. K., Zhang Y. High-entropy alloys. Springer: Cham. 2015.
1.34 Ye Y. F., Wang Q., Lu J., Liu C. T., Yang Y. High-entropy alloy: challenges and prospects. *Mater. Today*. 2016. V. 19. P. 349–362.
1.35 Senkov O. N., Miracle D. B., Chaput K. J., Couzinie J.-P. Development and exploration of refractory high entropy alloys – A review. *J. Mater. Res.* 2018. V. 33. P. 3092–3128.
1.36 George E. P., Raabe D., Ritchie R. O. High-entropy alloys. *Nat. Rev. Mater*. 2019. V. 4. P. 515–534.
1.37 Koželj P., Vrtnik S., Jelen A., Jazbec S., Jagličić Z., Maiti S., Feuerbacher M., Steurer W., Dolinšek J. Discovery of a superconducting high-entropy alloy. *Phys. Rev. Lett.* 2014. V. 113. P. 107001.
1.38 Mott N. F., Jones W. Theory of the properties of metals and alloys. Oxford University Press: Oxford. 1958.
1.39 Cossy-Favre A., Boyen H. G., Oelhafen P. Electronic structure of Nb_xMo_{100-x} solid solutions. *Phys. Rev. B.* 1995. V. 52. P. 16410.
1.40 Becker C., Hafner J. Electronic structure of crystalline and amorphous Nb_xMo_{1-x} alloys: Rigid versus rectangular bands. *J. Phys.: Condens. Matter*. 1995. V. 7. P. 5843.
1.41 Skorodumova N. V., Simak S. I., Abrikosov I. A., Johansson B., Vekilov Yu. Kh. Electronic topological transitions in Mo-Re random alloys. *Phys. Rev. B.* 1998. V. 57. P. 14673.
1.42 Anderson P. W. Localized magnetic states in metals. *Phys. Rev*. 1961. V. 124. P. 41.
1.43 Okada M., Rotenberg E., Kevan S. D., Schäfer J., Ujfalussy B., Stocks G. M., Genatempo B., Bruno E., Plummer E. W. Evolution of

the electronic structure in $Mo_{1-x}Re_x$ alloys. *New J. Phys.* 2013. V. 15. P. 093010.

1.44 Tarenkov V., Dyachenko A., Krivoruchko V., Shapovalov A., Belogolovskii M. Tunneling-spectroscopy evidence for two-gap superconductivity in a binary Mo-Re alloy. *J. Supercond. Nov. Magn*. 2020. V. 33. P. 569–574.

1.45 Tarenkov V., Shapovalov A., Boliasova O., Belogolovskii M., Kordyuk A. Two-band superconductivity in a Mo–Re alloy with an equal concentration of the components. *Low Temp. Phys*. 2021. V. 47. P. 101–105.

1.46 Lifshitz I. M. Anomalies of electron characteristics of a metal in the high pressure region *Sov. Phys. JETP*. 1960. V. 11. P. 1130–1135.

1.47 Lifshitz I. M., Azbel M. Ya., Kaganov M. I. Electron Theory of Metals. Consultant Bureau: New York. 1973.

1.48 Blanter Y. M., Kaganov M. I., Pantsulaya A. V., Varlamov A. A. The theory of electronic topological transitions. *Phys. Rep.* 1994. V. 245. P. 159–257.

1.49 Brandt N. B., Ginzburg N. I., Ignat'eva T. A., Lazarev B. G., Lazareva L. S., Makarov V. I. Influence of impurities on the effect of pressure on thallium. II. *J. Exp. Theor. Phys.* 1966. V. 22. P. 61–64.

1.50 Sharath Chandra L. S., Sundar S., Banik S., Ramjan S. K., Chattopadhyay M. K., Jha S. N., Roy S. B. Localization of electronic states resulting from electronic topological transitions in the $Mo_{1-x}Re_x$ alloys: A photoemission study. *J. Appl. Phys.* 2020. V. 127. P. 163906.

1.51 Davidson D. L., Brotzen F. R. Plastic deformation of molybdenum-rhenium alloy crystals. *Acta Metall.* 1970. V. 18. P. 463–470.

1.52 Smith H. G., Wakabayashi N., Mostoller M. Phonon anomalies in transition metals, alloys and compounds. In: Proceedings of Second Rochester Conference on Superconductivity in d- and f-band Metals. Ed. by Douglass D. H. Plenum Press: New York. 1976. P. 223–249.

1.53 Ignat'eva T. A. Electron localization during an electronic-topological transition in Mo-Re alloys. *Phys. Solid State.* 2007. V. 49. P. 403–412.

1.54 Sundar S., Chandra L. S., Chattopadhyay M. K., Roy S. B. Evidence of multiband superconductivity in the β-phase $Mo_{1-x}Re_x$ alloys. *J. Condens. Matter Phys.* 2015. V. 27. P. 045701.

1.55 Sundar S., Sharath Chandra L. S., Chattopadhyay M. K., Pandey S. K., Venkateshwarlu D., Rawat R., Ganesan V., Roy S. B. Strong electron–phonon coupling and multiband effects in the superconducting β-phase $Mo_{1-x}Re_x$ alloys. *New J. Phys.* 2015. V. 17. P. 053003.
1.56 Stewart G. R., Giorgi A. L. A search for strong coupling superconductivity. *Solid State Commun*. 1978. V. 28. P. 969–972.
1.57 Kim M. S., Skinta J. A., Lemberger T. R., Kang W. N., Kim H.-J., Choi E.-N., Lee S.-I. Reflection of a two-gap nature in penetration-depth measurements of MgB_2 film. *Phys. Rev. B*. 2002. V. 66. P. 064511.
1.58 Wolf E. L. Principles of electron tunneling spectroscopy, 2nd edn. Oxford University Press: New York. 2012.
1.59 Agraıt N., Yeyati A. L., Van Ruitenbeek J. M. Quantum properties of atomic-sized conductors. *Phys. Rep*. 2003. V. 377. P. 81–279.
1.60 Aono M., Hasegawa T. The atomic switch. *Proc. IEEE*. 2010. V. 98. P. 2228–2236.
1.61 Blonder G. E., Tinkham M., Klapwijk T. M. Transition from metallic to tunneling regimes in superconducting microconstrictions: Excess current, charge imbalance, and supercurrent conversion. *Phys. Rev. B.* 1982. V. 25. P. 4515.
1.62 Volkov S., Gregor M., Plecenik T., Zhitlukhina E., Belogolovskii M., Plecenik A. Above-gap differential conductance dips in superconducting point contacts. *Appl. Nanosci.* 2022. V. 12. P. 761–768.
1.63 Zhitlukhina E., Devyatov I., Egorov O., Belogolovskii M., Seidel P. Anomalous inner-gap structure in transport characteristics of superconducting junctions with degraded interfaces. *Nanoscale Res. Lett.* 2016. V. 11. P. 1–9.
1.64 Daghero D., Gonnelli R. S. Probing multiband superconductivity by point-contact spectroscopy. *Supercond. Sci. Technol.* 2010. V. 23. P. 043001.
1.65 Talvacchio J., Janocko M. A., Greggi J. Properties of evaporated Mo-Re thin-film superconductors. *J. Low Temp. Phys*. 1986. V. 64. P. 395–408.
1.66 Falge Jr R. L. Superconductivity of hexagonal beryllium. *Phys. Lett. A*. 1967. V. 24. P. 579–580.
1.67 Curzon A. E., Mascall A. J. Superconductivity in thin films of beryllium. *J. Phys. C*. 1969. V. 2. P. 382.

1.68 Granqvist C. G., Claeson T. Superconductivity of vapour quenched beryllium and beryllium-based alloys. Z. *Phys. B Con. Mat.* 1975. V. 20. P. 13–20.
1.69 Flasck J., Wood J., Edelstein A. S., Keem J. E., Missell F. P. Superconducting properties of amorphous transition metal alloys. *Solid State Commun*. 1982. V. 44. P. 649–652.
1.70 Bandyopadhyay S., Ganguly S. The effect of disorder on electronic structure and conducting properties of superconductors with various kinds of pairing symmetries. In *2019 International Conference on Opto-Electronics and Applied Optics (Optronix)*. *IEEE*. 2019.
1.71 Komnik Y. F. Electrical properties of fine crystalline and amorphous metal films, obtained by low temperature condensation (Review). *Sov. J. Low Temp. Phys*. 1982. V. 8. P. 57–78.
1.72 Wright A. C. The great crystallite versus random network controversy: a personal perspective. *Int. J. Appl. Glass Sci*. 2014. V. 5. P. 31–56.
1.73 Mavračić J., Mocanu F. C., Deringer V. L., Csányi G., Elliott S. R. Similarity between amorphous and crystalline phases: the case of TiO_2. *J. Phys. Chem. Lett.* 2018. V. 9. P. 2985–2990.
1.74 Guillamón I., Suderow H., Fernández-Pacheco A., Sesé J., Córdoba R., De Teresa J. M., Ibarra M. R., Vieira S. Direct observation of melting in a two-dimensional superconducting vortex lattice. *Nat. Phys.* 2009. V. 5. P. 651–655.
1.75 Roy I., Dutta S., Roy Choudhury A. N., Basistha S., Maccari I., Mandal S., Jesudasan J., Bagwe V., Castellani C., Benfatto L., Raychaudhuri P. Melting of the vortex lattice through intermediate hexatic fluid in an a− MoGe thin film. *Phys. Rev. Lett*. 2019. V. 122. P. 047001.
1.76 Natarajan C. M., Tanner M. G., Hadfield R. H. Superconducting nanowire single-photon detectors: physics and applications. *Supercond. Sci. Technol*. 2012. V. 25. P. 063001.
1.77 Banerjee A., Baker L. J., Doye A., Nord M., Heath R. M., Erotokritou K., Bosworth D., Barber Z. H., MacLaren I., Hadfield R. H. Characterisation of amorphous molybdenum silicide (MoSi) superconducting thin films and nanowires *Supercond. Sci. Technol*. 2017. V. 30. P. 084010.

1.78 Miyahara K., Mukaida M., Tokumitsu M., Kubo S., Hohkawa K. Abrikosov vortex memory with improved sensitivity and reduced write current levels. *IEEE Trans. Magn.* 1987. V. 23. P. 875–878.
1.79 Holzman I., Ivry Y. Superconducting nanowires for single-photon detection: Progress, Challenges, and Opportunities. *Adv. Quantum Technol.* 2019. V. 2. P. 1800058.
1.80 Yu L. Superconducting nanowire single-photon detectors for quantum information. *Nanophotonics.* 2020. V. 9. P. 2673–2692.
1.81 Semenov A. D. Superconducting nanostrip single-photon detectors: some fundamental aspects in detection mechanism, technology and performance. *Supercond. Sci. Technol*. 2021. V. 34. P. 054002.
1.82 Lehtinen J. S., Kemppinen A., Mykkänen E., Prunnila M., Manninen A. J. Superconducting MoSi nanowires. *Supercond. Sci. Technol.* 2017. V. 31. P. 015002.
1.83 Mooij J. E., Nazarov Y. V. Superconducting nanowires as quantum phase-slip junctions *Nature Phys.* 2006. V. 2. P. 169–172.
1.84 Murphy A., Averin D. V., Bezryadin A. Nanoscale superconducting memory based on the kinetic inductance of asymmetric nanowire loops. *New J. Phys*. 2017. V. 19. P. 063015.
1.85 Singh A., Voltan S., Lahabi K., Aarts J. Colossal proximity effect in a superconducting triplet spin valve based on the half-metallic ferromagnet CrO_2. *Phys. Rev. X*. 2015. V. 5. P. 021019.
1.86 Dausy H., Nulens L., Raes B., Van Bael M. J., Van de Vondel J. Impact of kinetic inductance on the critical-current oscillations of nanobridge SQUIDs. *Phys. Rev. Appl.* 2021. V. 16. P. 024013.
1.87 Douçot B., Ioffe L. B. Physical implementation of protected qubits. *Rep. Prog. Phys.* 2012. V. 75. P. 072001.
1.88 Nevirkovets I. P., Belogolovskii M. A., Ketterson J. B. Josephson junctions based on amorphous MoGe: Prospects for use in superconducting electronics. *Supercond. Sci. Technol*. 2022 V. 35. P. 035008.
1.89 Wolf E., Arnold G., Gurvitch M., Zasadzinski J. Josephson junctions: History, devices, and applications. Pan Stanford Publ.: Singapore. 2017. Ch. 5.

1.90 Miller R. E., Mallison W. H., Kleinsasser A. W., Delin K. A., Macedo E. M. Niobium trilayer tunnel junctions with ultrahigh critical-current densities. *Appl. Phys. Lett.* 1993. V. 63. P. 1423–425.
1.91 Tolpygo S. K., Semenov V. K. Increasing integration scale of superconductor electronics beyond one million Josephson junctions. *J. Phys.: Conf. Ser*. 2020. V. 1559. P. 012002.
1.92 Kwo J., Wertheim G. K., Gurvitch M., Buchanan D. N. X-ray photoemission spectroscopy study of surface oxidation of Nb/Al overlayer structures. *Appl. Phys. Lett.* 1982. V. 40. P. 675–677.
1.93 Kleinsasser A. W., Rammo F. M., Bhushan M. Degradation of superconducting tunnel junction characteristics with increasing barrier transparency. *Appl. Phys. Lett.* 1993. V. 62. P. 1017–1019.
1.94 Belogolovskii M., Zhitlukhina E., Lacquaniti V., De Leo N., Fretto M., Sosso A. Intrinsically shunted Josephson junctions for electronics applications. *Low Temp. Phys*. 2017. V. 43. P. 756–765.
1.95 Seidel P., Richter J. Theoretical investigation of the current-voltage characteristics of superconducting niobium-lead tunnel junctions. *Phys. Stat. Solidi. B.* 1980. V. 98. P. 189–197.
1.96 Köhler H. J., Seidel P., Weber P., Blüthner K., Linke S., Berthel K. H. Influence of the niobium base electrode on the temperature dependence of the effective niobium energy gap and the critical Josephson current in Nb-NbO_x-Pb tunnel junctions. *Phys. Stat. Solidi. A.* 1981. V. 67. P. 497–503.
1.97 Nguyen L., Hashimoto T., Zakharov D. N., Stach E. A., Rooney A. P., Berkels B., Thompson G. E., Haigh S. J., Burnett T. L. Atomic-scale insights into the oxidation of aluminum. *ACS Appl. Mater. Interfaces*. 2018. V. 10. P. 2230–2235.
1.98 Aykol M., Persson K. A. Oxidation protection with amorphous surface oxides: thermodynamic insights from ab initio simulations on aluminum. *ACS Appl. Mater. Interfaces*. 2018. V. 10. P. 3039–3045.
1.99 Cai N., Zhou G., Mueller K., Starr D. E. Effect of oxygen gas pressure on the kinetics of alumina film growth during the oxidation of Al(111) at room temperature. *Phys. Rev. B.* 2011. V. 84. P. 125445.

1.100 Flototto D., Wang Z. M., Jeurgens L. P. H., Mittemeijer E. J. Intrinsic stress evolution during amorphous oxide film growth on Al surfaces. *Appl. Phys. Lett*. 2014. V. 104. P. 091901.
1.101 Svistunov V. M., D'yachenko A. I., Belogolovskii M. A. Elastic tunneling spectroscopy of single-particle excitations in metals. *J. Low Temp. Phys*. 1978. V. 31. P. 339–356.
1.102 Dynes R. C., Garno J. P., Hertel G. B., Orlando T. P. Tunneling study of superconductivity near the metal-insulator transition. *Phys. Rev. Lett*. 1984. V. 53. P. 2437–2440.
1.103 Tashiro H., Graybeal J. M., Tanner D. B., Nicol E. J., Carbotte J. P., Carr G. L. Unusual thickness dependence of the superconducting transition of α-MoGe thin films. *Phys. Rev. B.* 2008. V. 78. P. 014509.
1.104 Elesin V. F., Kopaev Yu. V. Superconductors with excess quasiparticles. *Sov. Phys. Usp*. 1981. V. 24. P. 116–141.
1.105 Nevirkovets I. P., Chernyashevskyy O., Prokopenko G. V., Mukhanov O. A., Ketterson J. B. Superconducting-ferromagnetic transistor. *IEEE Trans. Appl. Supercond*. 2014. V. 24. P. 1800506.
1.106 Nevirkovets I. P., Chernyashevskyy O., Prokopenko G. V., Mukhanov O. A., Ketterson J. B. Control of supercurrent in hybrid superconducting–ferromagnetic transistors. *IEEE Trans. Appl. Supercond*. 2015. V. 25. P. 1800705.
1.107 Parker W. H. Modified heating theory of nonequilibrium superconductors. *Phys. Rev. B.* 1975. V. 12. P. 3667–3672.
1.108 Gulian A., Dulal R., Teknowijoyo S., Chahid S. Dialogue on a superconducting laser operating via nonequilibrium inversed population. *Modern Phys. Lett. B.* 2020. V. 34. P. 2030005.
1.109 Liang M., Kunchur M. N. Vortex instability in molybdenum-germanium superconducting films. *Phys. Rev. B.* 2010. V. 82. P. 144517.
1.110 Kaplan S. B., Chi C., Langenberg D. N., Chang J. J., Jafarey S., Scalapino D. J. Quasiparticle and phonon lifetimes in superconductors. *Phys. Rev. B.* 1976. V. 14. P. 4854–4873.
1.111 Gershenson M. E., Gubankov V. N. Gap relaxation time in superconducting Nb films. *Physica.* 1981. V. 108B. P. 971–972.

1.112 Bezryadin A. Superconductivity in nanowires: Fabrication and quantum transport, Wiley-VCH: Weinheim. 2013.
1.113 Gladstone G., Jensen M. A., Schrieffer J. R. Superconductivity in the transition metals: Theory and experiment. In: *Superconductivity*. Vol. 2. Ed. by Parks R. D. M. Dekker: New York. 1969. Ch. 13.
1.114 Barone A., Paterno G. Physics and applications of the Josephson effect. Wiley: *Hoboken*. 1982.
1.115 Enpuku K., Yoshida K., Hamasaki K., Irie F. Effects of microshorts on current-voltage characteristics of Josephson tunnel junctions. *JJAP*. 1981. V. 20. P. 265.
1.116 Kojima S., Sato H., Yosihara A. Light scattering of supercooled propylene glycol. *J. Phys.: Condens. Matter*. 1997. V. 9. P. 10079.
1.117 Nakayama T. Boson peak and terahertz frequency dynamics of vitreous silica. *Rep. Prog. Phys.* 2002. V. 65. P. 1195.
1.118 Hu Y. C., Tanaka H. Origin of the boson peak in amorphous solids. *Nat. Phys*. 2022. P. 1–9.
1.119 Combescot R. Strong-coupling limit of Eliashberg theory. *Phys. Rev. B.* 1995. V. 51. P. 11625–11634.
1.120 Marsiglio F. Eliashberg theory: A short review. *Ann. Phys.* 2000. V. 417. P. 168102.
1.121 Baggioli M., Setty C., Zaccone A. Effective theory of superconductivity in strongly coupled amorphous materials. *Phys. Rev. B.* 2020. V. 101. P. 214502.
1.122 Pettit R. B., Silcox J. Film structure and enhanced superconductivity in evaporated aluminum films. *Phys. Rev. B.* 1976. V. 13. P. 2865–2872.
1.123 Knorr K., Barth N. Electron tunneling into disordered thin films. *J. Low Temp. Phys*. 1971. V. 4. P. 469–484.
1.124 Bergmann G., Rainer D. The sensitivity of the transition temperature to changes in $\alpha^2F(\omega)$. *Z. Phys*. 1973. V. 263. P. 59–68.
1.125 Dayan M. Tunneling measurements on crystalline and granular aluminum. *J. Low Temp. Phys*. 1978. V. 32. P.643.
1.126 Kamiya K., Takeuchi T., Kabeya N., Wada N., Ishimasa T., Ochiai A., Deguchi K., Imura K., Sato N. K. Discovery of superconductivity in quasicrystal. *Nat. Commun.* 2018. V. 9. P. 1–8.

1.127 Kimura K., Iwahashi H., Hashimoto T., Takeuchi S., Mizutani U., Ohashi S., Itoh G. Electronic properties of the single-grained icosahedral phase of Al–Li–Cu. *J. Phys. Soc. Japan.* 1989. V. 58. P. 2472–2481.
1.128 Mizutani U., Sakabe Y., Shibuya T., Kishi K., Kimura K., Takeuchi S. Electron transport properties of thermodynamically stable Al-Cu-Ru icosahedral quasicrystals. *J. Phys. Condens. Matter.* 1990. V. 2. P. 6169.
1.129 Deguchi K., Matsukawa S., Sato N.K., Hattori T., Ishida K., Takakura H., Ishimasa T. Quantum critical state in a magnetic quasicrystal. *Nat. Mater.* 2012. V. 11. P. 1013–1016.
1.130 Liu Y. B., Hao J. J., Zhang Y., Cao Y., Chen W. Q., Yang F. Cooper instability and superconductivity of the Penrose lattice. *Sci. China Phys. Mech.* 2022. V. 65. P. 1–11.
1.131 Takemori N., Arita R., Sakai S. Physical properties of weak-coupling quasiperiodic superconductors. *Phys. Rev. B.* 2020. V. 102. P. 115108.
1.132 Zhang Y., Zuo T., Tang Z., Gao M. C., Dahmen K. A., Liaw P. K., Lu Z. Microstructures and properties of high-entropy alloys. *Prog. Mater. Sci*. 2014. V. 61. P. 1–93.
1.133 Miracle D. B., Senkov O. N. A critical review of high entropy alloys and related concepts. *Acta. Mater.* 2017. V. 122. P. 448–511.
1.134 Yeh J.-W., Chen S.-K., Lin S.-J., Gan J.-Y., Chin T.-S., Shun T.-T., Tsau C.-H., Chang S.-Y. Nanostructured high-entropy alloys with multiple principal elements: Novel alloy design concepts and outcomes. *Adv. Eng. Mater*. 2004. V. 6. P. 299–303.
1.135 Otto F., Yang Y., Bei H., George E. P. Relative effects of enthalpy and entropy on the phase stability of equiatomic high-entropy alloys. *Acta Mater.* 2013. V. 61. P. 2628–2638.
1.136 Sun L., Cava R. J. High-entropy alloy superconductors: Status, opportunities, and challenges. *Phys. Rev. Mater*. 2019. V. 3. P. 090301.
1.137 Kitagawa J., Hamamoto S., Ishizu N. Cutting edge of high-entropy alloy superconductors from the perspective of materials research. *Metals*. 2020. V. 10. P. 1078.
1.138 Kitagawa J., Ishizu N., Hamamoto S. Materials research on high-entropy alloy superconductors. In: *Advances in High-Entropy Alloys-*

Materials Research, Exotic Properties and Applications. IntechOpen: London. 2021.

1.139 Stolze K., Tao J., von Rohr F. O., Kong T., Cava R. J. Sc–Zr–Nb–Rh–Pd and Sc–Zr–Nb–Ta–Rh–Pd high-entropy alloy superconductors on a CsCl-type lattice. *Chem. Mater.* 2018. V. 30. P. 906–914.

1.140 Mizuguchi Y., Kasem M. R., Matsuda T. D. Superconductivity in $CuAl_2$-type $Co_{0.2}Ni_{0.1}Cu_{0.1}Rh_{0.3}Ir_{0.3}Zr_2$ with a high-entropy-alloy transition metal site. *Mater. Res. Lett.* 2021. V. 9. P. 141–147.

1.141 Kasem M. R., Yamashita A., Goto Y., Matsuda T. D., Mizuguchi Y. Synthesis of high-entropy-alloy-type superconductors (Fe, Co, Ni, Rh, Ir) Zr_2 with tunable transition temperature. *J. Mater. Sci.* 2021. V. 56. P. 9499–9505.

1.142 Charifoulline Z. Residual resistivity ratio (RRR) measurements of LHC superconducting NbTi cable strands. *IEEE Trans. Appl. Supercond*. 2006. V. 16. P. 1188–1191.

1.143 Matthias B. T. Empirical relation between superconductivity and the number of valence electrons per atom. *Phys. Rev*. 1955. V. 97. P. 74–76.

1.144 Hott R., Kleiner R., Wolf T., Zwicknagl G. Review on superconducting materials. In: Applied Superconductivity. Handbook on Devices and Applications. V. 1. Ed. P. Seidel. Wiley-VCH: Weinheim. P. 26–48.

1.145 von Rohr F., Winiarski M. J., Tao J., Klimczuk T., Cava R. J. Effect of electron count and chemical complexity in the Ta-Nb-Hf-Zr-Ti high-entropy alloy superconductor. *Proc. Natl. Acad. Sci. USA*. 2016. V. 113. P. E7144–E7150.

1.146 Guo J., Wang H., von Rohr F., Wang Z., Cai S., Zhou Y., Yang K., Li A., Jiang S., Wu Q., Cava R. J., Sun L. Robust zero resistance in a superconducting high-entropy alloy at pressures up to 190 GPa. *Proc. Natl. Acad. Sci. USA*. 2017. V. 114. P. 13144–13147.

1.147 Vrtnik S., Koželj P., Meden A., Maiti S., Steurer W., Feuerbacher M., Dolinšek J. Superconductivity in thermally annealed Ta-Nb-Hf-Zr-Ti high-entropy alloys. *J. Alloys Compd*. 2017. V. 695. P. 3530–3540.

1.148 Zhang X., Winter N., Witteveen C., Moehl T., Xiao Y., Krogh F., Schilling A., von Rohr F. O. Preparation and characterization of high-entropy alloy $(TaNb)_{1-x}(ZrHfTi)_x$ superconducting films. *Phys. Rev. Res*. 2020. V. 2. P. 013375.

1.149 Lee Y.-S., Cava R. J. Superconductivity in high and medium entropy alloys based on MoReRu. *Phys. C*. 2019. V. 566. P. 1353520.
1.150 Islam N., Huang W., Zhuang H. L. Machine learning for phase selection in multi-principal element alloys. *Comput. Mater. Sci*. 2018. V. 150. P. 230–235.
1.151 Li Y., Guo W. Machine-learning model for predicting phase formations of high-entropy alloys. *Phys. Rev. Mater*. 2019. V. 3. P. 095005.
1.152 Lu Y., Dong Y., Guo S., Jiang L., Kang H., Wang T., Wen B., Wang Z., Jie J., Cao Z., Ruan H., Li T. A promising new class of high-temperature alloys: Eutectic high-entropy alloys. *Sci. Rep*. 2015. V. 4. P. 6200.
1.153 Zherebtsov S., Yurchenko N., Panina E., Tikhonovsky M., Stepanov N. Gum-like mechanical behavior of a partially ordered $Al_5Nb_{24}Ti_{40}V_5Zr_{26}$ high entropy alloy. *Intermetallics*. 2020. V. 116. P. 106652.
1.154 Yuan S., Lin N., Zeng Q., Zhang H., Wu Y. Recent advances in gum metal: Synthesis, performance and application. *Crit. Rev. Solid State Mater. Sci*. 2022. P. 1–32.
1.155 Neverov V. D., Lukyanov A. E., Krasavin A. V., Vagov A., Croitoru M. D. Correlated disorder as a way towards robust superconductivity. *Commun Phys.* 2022. V. 5. P. 177.